Check for updates

JGR Atmospheres

RESEARCH ARTICLE
10.1029/2024JD042102

The Cold Bias in the Surface Air Temperature Simulations Over the Tibetan Plateau of RegCM4 Reduced by Adopting the 3D Sub-Grid Terrain Longwave Radiative Effect Scheme

Chunlei Gu[1], **Anning Huang**[1,2], **Xin Li**[3], **and Yang Wu**[3]

[1]School of Atmospheric Sciences, Nanjing University, Nanjing, China, [2]Qinghai Lake Comprehensive Observation Research Station, Chinese Academy of Sciences, Gangcha, China, [3]Key Laboratory of Transportation Meteorology of China Meteorological Administration, Nanjing Joint Institute for Atmospheric Sciences, Chinese Academy of Meteorological Sciences—Jiangsu Meteorological Service, Nanjing, China

Abstract The 3D sub-grid terrain longwave radiative effects (3DSTLRE), which significantly regulate the surface downward longwave radiation (SDLR) in the mountainous regions, are not described in current numerical models. We incorporated a 3DSTLRE scheme into RegCM4 to assess its influence on modeling the surface air temperature (SAT) across the Tibetan Plateau (TP). Results show that the RegCM4 adopting the parallel-plane longwave radiative scheme significantly underestimates the SAT over TP, this underestimation of SAT is clearly mitigated by considering 3DSTLRE, with the root mean square error (RMSE) decreased by 9%. The SAT simulations are improved more noticeable over western TP than entire TP and more evident at nighttime than at daytime in different seasons. Further analysis indicates that the improvement of SAT simulations over the rugged areas of TP is primarily benefited from the improved SDLR simulations. In the absence of the 3DSTLRE scheme, RegCM4 markedly underestimates SDLR by 20 $W \cdot m^{-2}$ over the entire TP, this underestimation can be greatly reduced by 15 $W \cdot m^{-2}$ through adopting the 3DSTLRE scheme, with the RMSE reduced by more than 40% over the rugged edges of TP. The increased SDLR induced by the 3DSTLRE is mainly transformed into sensible heat flux to warm the near surface air, further leading to reduced cold bias of SAT produced by the RegCM4 without 3DSTLRE. Better representing the TP thermal condition can enhance the simulation of East Asian monsoon. Therefore, incorporating the 3DSTLRE scheme in numerical models can potentially improve the ability in simulating and predicting the East Asian monsoon.

Plain Language Summary The terrain significantly affects the surface downward longwave radiation (SDLR). Currently, most numerical models do not describe in the impact of terrain on SDLR. This research integrated the effects of terrain on SDLR into RegCM4 and revealed its effect on the model ability to simulate the surface air temperature (SAT) over the Tibetan Plateau (TP) based on sensitivity experiments. Results show that the original RegCM4 significantly underestimates the SDLR and SAT in the TP. Including the impact of terrain on SDLR in the RegCM4 can improve the SDLR and SAT simulations over the rugged areas by mitigating their underestimations. The increased SDLR over the rugged areas primarily comes from the longwave radiation emitted from the surrounding terrains. The increased SDLR further warms the ground surface and generate more sensible heat flux and thereafter increased SAT. Overall, considering the impact of terrain on SDLR in numerical models may be an efficient way to improve the simulations of SAT over rugged areas.

Key Points:

- The 3DSTLRE scheme obviously improve surface downward longwave radiation (SDLR) underestimated by the RegCM4 over the Tibetan Plateau
- The improved surface SDLR simulation helps reduce the cold bias in the surface air temperature simulations of RegCM4 in the Tibetan Plateau
- Considering the 3DSTLRE in numerical models may be an efficient way to improve the surface air temperature simulations over rugged areas

Correspondence to:
A. Huang,
Anhuang@nju.edu.cn

Citation:
Gu, C., Huang, A., Li, X., & Wu, Y. (2024). The cold bias in the surface air temperature simulations over the Tibetan Plateau of RegCM4 reduced by adopting the 3D sub-grid terrain longwave radiative effect scheme. *Journal of Geophysical Research: Atmospheres*, *129*, e2024JD042102. https://doi.org/10.1029/2024JD042102

Received 5 AUG 2024
Accepted 17 NOV 2024
Corrected 30 DEC 2024

This article was corrected on 30 DEC 2024. See the end of the full text for details.

Author Contributions:
Conceptualization: Anning Huang
Data curation: Chunlei Gu, Xin Li, Yang Wu
Formal analysis: Chunlei Gu
Investigation: Chunlei Gu, Anning Huang, Xin Li
Methodology: Chunlei Gu, Anning Huang, Xin Li
Resources: Chunlei Gu, Xin Li, Yang Wu
Software: Chunlei Gu, Yang Wu
Supervision: Anning Huang
Validation: Chunlei Gu, Xin Li
Visualization: Chunlei Gu
Writing – original draft: Chunlei Gu, Anning Huang
Writing – review & editing: Chunlei Gu, Anning Huang, Xin Li, Yang Wu

© 2024. American Geophysical Union. All Rights Reserved.

1. Introduction

The Tibetan Plateau (TP) is one of the most complex terrain areas in the world and is highly sensitive to the effects of global warming (You et al., 2021). The surface air temperature (SAT) over the TP has exhibited unique features in the past decades, such as an increasing warming rate with elevation and a reduced annual temperature cycle (Niu et al., 2021; Palazzi et al., 2017). The warming SAT and thermal conditions over the TP have significant impacts on regional and global climates through complex processes (Diallo et al., 2022; Hu et al., 2023).

Numerical models are important tools for climate studies, and accurate simulation of the SAT over the TP is necessary (Wang et al., 2018; Wu et al., 2022). However, the numerical models commonly exhibit a noticeable cold bias of SAT simulations in the TP, especially over the western part of the TP with much more complex sub-grid terrains during dry seasons (Fan et al., 2020; Gao et al., 2015; Hu et al., 2022; Niu et al., 2021; Su et al., 2013;

21698996, 2024, 23, Downloaded from https://agupubs.onlinelibrary.wiley.com/doi/10.1029/2024JD042102 by Nanjing University, Wiley Online Library on [19/06/2025]. See the Terms and Conditions (https://onlinelibrary.wiley.com/terms-and-conditions) on Wiley Online Library for rules of use; OA articles are governed by the applicable Creative Commons License

M. Zhou et al., 2023). Ma et al. (2023) and P. Zhou et al. (2023) suggest that employing the Weather Research and Forecasting model at a very high resolution may mitigate the cold bias issue in the TP. However, Zhu et al. (2019) and Guo et al. (2020) suggest that the dynamic downscaling of reanalysis data or the outputs from global climate models may exacerbate the cold bias over the TP. Similar to other numerical models, the Regional Climate Model Version 4 (RegCM4) significantly underestimates the SAT in the TP (Gao et al., 2017; Ge et al., 2021; Liang et al., 2019; Ren et al., 2023; Yang et al., 2018; Yu et al., 2020).

Improving the simulation of SAT should prioritize the precise representation of physical processes, rather than merely increasing the resolution of numerical models (Wang et al., 2023; Xu et al., 2019). Previous studies (Luo et al., 2023; Sun et al., 2023; Yue et al., 2021; X. Zhou et al., 2023, 2022) show that enhancing the representation of the physical processes related to soil, vegetation, and land-atmosphere energy exchange in the numerical models can improve the accuracy of SAT simulations in the TP. An inadequate portrayal of the land surface radiation balance is identified as a key element that contributes to the underestimation of SAT in the TP (Lee, Li, et al., 2019; Lee, Liou, 2019). Some studies indicate that the underestimated SAT in the TP can be attributed to the overestimated surface albedo and underestimated surface downwelling longwave radiation (SDLR, An et al., 2022; Chen et al., 2017; Wang et al., 2023; X. Zhou et al., 2023).

The limitations of numerical models in accurately simulating clouds and their radiative forcing represent the most significant source of error in modeling the SDLR (Jiang et al., 2023; Li et al., 2024; Viúdez-Mora et al., 2015). The RegCM4 also faces challenges related to inadequate cloud simulation capabilities, which lead to uncertainty in the simulated SDLR (H. Gu et al., 2020; Pareja-Quispe et al., 2021). To improve the simulation of clouds and precipitation, Nogherotto et al. (2016) introduced a novel cloud microphysics scheme to the RegCM4. However, the new Regional Climate Model Version 5, which incorporates the Nogherotto cloud scheme and utilizes ECMWF Reanalysis v5 forcing data, continues to underestimate the cloud liquid water and SAT over the TP (Coppola et al., 2024). In rugged areas, overlooking the impact of the terrain on the SDLR is another significant source of simulating errors of the SDLR.

Complex topography substantially influences the SDLR by obstructing the atmospheric infrared radiation and by emitting its own infrared radiation onto the target surface (Dozier & Outcalt, 1979; Duguay, 1995). The atmospheric infrared radiation obstructed by terrain is commonly weaker than that emitted from the surrounding terrain, resulting in relatively higher SDLR over the rugged areas than over the plane surface (Whiteman & Hoch, 2010; Wu et al., 2019). Neglecting the longwave radiative effects of terrain may lead to the average (instantaneous) intensity of SDLR underestimated by several watts to several tens of watts (hundreds of watts) per square meter in the middle latitudes (Aubry-Wake et al., 2018; Feldman et al., 2022; Olyphant, 1986; Yan et al., 2020; Zhu et al., 2018).

The importance of describing the sub-grid terrain radiative effects in the numerical models has long been recognized since the 2000s (Colette et al., 2003; Zhang et al., 2002). A lot of parameterizations have been developed to depict the effects of sub-grid scale terrain on surface radiation and have been incorporated into various numerical models (Arthur et al., 2018; Gu et al., 2022; A. Huang et al., 2022; Lee et al., 2011; Zhang et al., 2006). Considering the impacts of sub-grid terrain on longwave radiation into numerical models can improve the description of surface energy balance (C. Gu et al., 2020; Zhang et al., 2006). However, these two studies totally neglect the longwave radiation emitted from the surrounding terrains, and to solve this issue, we have developed a parameterization scheme to completely describe the three-dimensional sub-grid terrain longwave radiative effects (3DSTLRE) (Gu et al., 2024).

The impact of long-wave radiation from three-dimensional structure of sub-grid terrains has been utilized in snow cover modeling, glacier simulations, and hydrological models to enhance temperature simulations (Arnold et al., 2006; Moore et al., 1993; Robledano et al., 2022; Sicart et al., 2006). However, these applications are restricted to very small spatial areas and shorter time frames. The impact of the 3DSTLRE scheme on SAT simulations in different seasons across a broader range remains unclear.

In this study, the 3DSTLRE scheme (Gu et al., 2024) was incorporated into RegCM4 to enhance its ability to describe the surface radiative balance. Despite of the significant influence of the thermal conditions of the TP on the climate of East Asia (Hao et al., 2023; Huang et al., 2023), this study has narrowed its research focus to the TP region. This approach aims to mitigate the effects of atmospheric circulation feedback and to better highlight the local influence of 3DSTLRE on the SAT over the TP. Three questions are raised: (a) To what extent can the

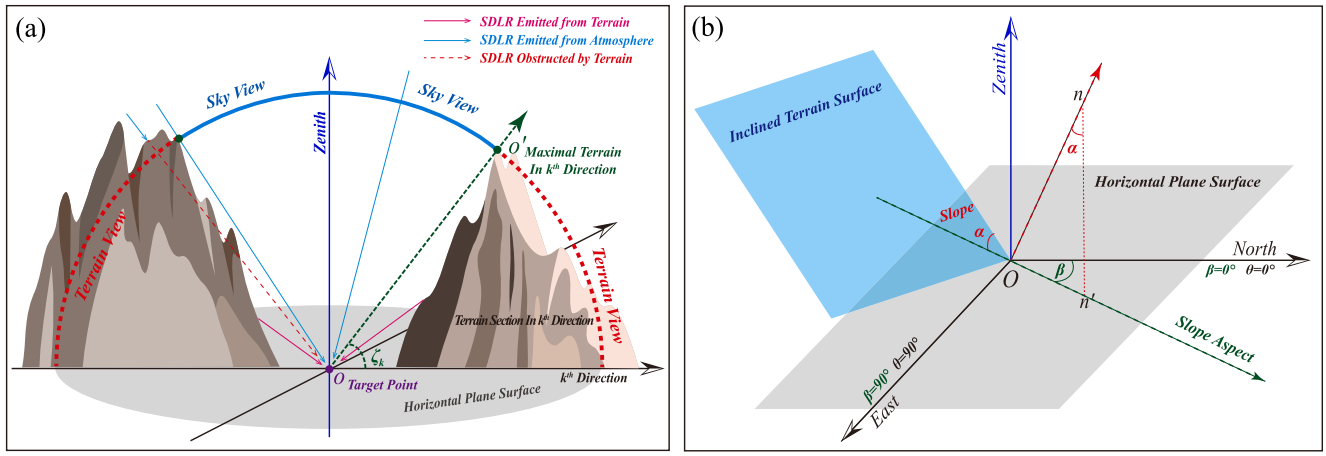

Figure 1. Schematic diagram of the sky view, the terrain view, the maximal topography elevation angle ζ_k, the surface downward longwave radiation flux (a), and the slope α (b) in the mountainous areas.

3DSTLRE improve the SDLR and SAT simulations across various seasons in large areas with complex terrain? (b) Can the cold bias of RegCM4 over the TP be mitigated by implementing the 3DSTLRE scheme? (c) What are the underlying physical mechanisms? Section 2 introduces the 3DSTLRE scheme, the RegCM4, the experimental design, the data, and the metrics for model evaluation. The results are shown in Section 3. Section 4 explores the potential physical mechanism. Section 5 gives the conclusions.

2. 3DSTLRE Scheme, RegCM4, Model Configuration, Data and Methodology

2.1. The 3DSTSRE Scheme

As shown in Figure 1a, the SDLR over the rugged terrains consists of two components: the SDLR from the atmosphere and the SDLR emitted from the surrounding terrains. The surrounding terrains block the atmosphere-emitted SDLR and emit long-wave radiation to the target surface at the same time. To describe the 3DSTLRE in numerical models, the 3DSTLRE scheme is implemented in three steps (Gu et al., 2024): (a) Calculate the sky view factor SVF_i and the terrain slope α_i of the sub-grids; (b) Calculate the grid-scale 3DSTLRE correction factors (C_1 and C_2) based on Equations 1 and 2; (c) Calculate the grid-scale SDLR ($L_{t,g\downarrow}$) with the consideration of 3DSTLRE based on Equation 3 with the C_1, C_2, $L_{p,g\downarrow}$, and $L_{p,g\uparrow}$.

$$C_1 = \left(\sum_{i=1}^{i=N} \mathrm{SVF}_i \cdot \sec \alpha_i\right) \Big/ \left(\sum_{i=1}^{i=N} \sec \alpha_i\right) \tag{1}$$

$$C_2 = \left[\sum_{i=1}^{i=N} (1 - \mathrm{SVF}_i) \cdot \sec \alpha_i\right] \Big/ \left(\sum_{i=1}^{i=N} \sec \alpha_i\right) \tag{2}$$

$$L_{t,g\downarrow} = L_{p,g\downarrow} \cdot C_1 + L_{p,g\uparrow} \cdot C_2 \tag{3}$$

where the $L_{p,g\downarrow}$ and $L_{p,g\uparrow}$ are the plane surface downwelling and upward longwave radiation fluxes at the model grid g, which are already calculated by the plane-parallel longwave radiative scheme. C_1 and C_2 are the terrain correction factors of the 3DSTLRE scheme at the grid-scale. The subscript t, p, i, and g represent the terrain surface, the plane surface, the sub-grid, and the grid, respectively. SVF and α are the sky view factor and terrain slope. The method to calculate the sky view factor (SVF) and the terrain slope can be found in Gu et al. (2024). The SVF represents the degree of sky openness at the target point (Figure 1a). (1 − SVF) represents the terrain view factor. The terrain slope ranging from 0° to 90° denotes the steepness of the terrain (Figure 1b). Larger terrain slope indicates steeper terrain. The SVF is dimensionless and ranges from 0.0 to 1.0. Smaller SVF indicates that larger fraction of the sky over the target point is obstructed by the topographies (Lindberg & Grimmond, 2010). C_1 (C_2) is the grid-scale sky (terrain) view factor. C_1 plus C_2 is equal to 1.0 (Figures 2a and 2b). Smaller C_1 and larger C_2 mean that a smaller proportion of the SDLR originates from the atmosphere, while a

21698996, 2024, 23, Downloaded from https://agupubs.onlinelibrary.wiley.com/doi/10.1029/2024JD042102 by Nanjing University, Wiley Online Library on [19/06/2025]. See the Terms and Conditions (https://onlinelibrary.wiley.com/terms-and-conditions) on Wiley Online Library for rules of use; OA articles are governed by the applicable Creative Commons License

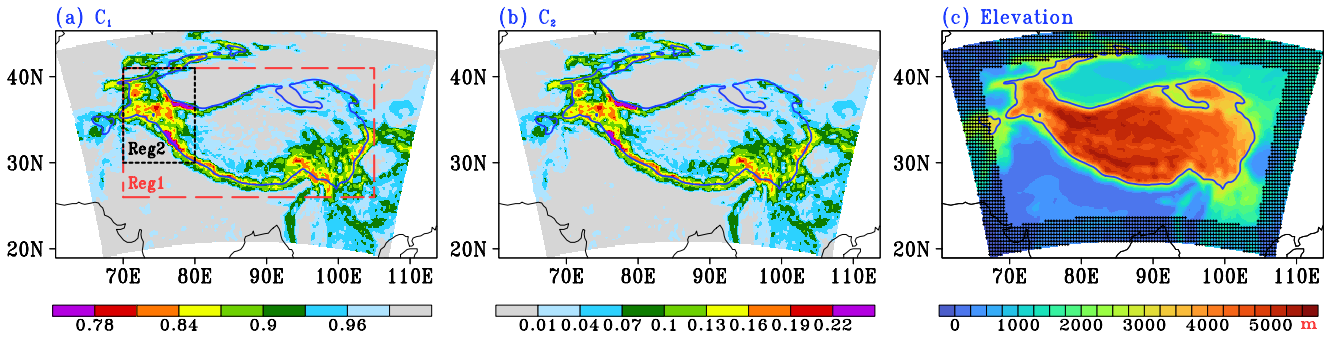

Figure 2. Spatial distributions of (a) sky view factor C_1, (b) terrain view factor C_2, and (c) topography at the grid-scale of 30 km. The dashed rectangles in (a) show the study areas. The black grids in (c) indicate the lateral buffer zone. The altitude of 3,000 m is shown as the blue solid lines.

larger proportion comes from the longwave radiation emitted from surrounding terrains. Therefore, smaller C_1 and larger C_2 indicate that the sub-grid terrains have stronger effects on the grid-scale SDLR. More details of the 3DSTLRE scheme can be found in the study of Gu et al. (2024). This study utilizes the terrain elevation data with an approximate spatial resolution of 90 m (Jarvis et al., 2008) to depict the sub-grid topographical features.

2.2. RegCM4

In this study, we adopted the RegCM4, which is provided and maintained by the Abdus Salam ICTP (Giorgi et al., 2012). It offers a wide range of parameterization options for physical processes and enables simulations with high horizontal resolution across areas characterized by intricate landscapes (Abish & Arun, 2019; Nogherotto et al., 2016). Consequently, the RegCM4 has emerged as a widely utilized regional climate model across Asia (Gao & Giorgi, 2017; Wu et al., 2024). However, like other numerical models, RegCM4 also adopts the plane-parallel longwave radiative scheme and neglects the 3DSTLRE.

2.3. Numerical Experiments

The RegCM4 has been modified to include the 3DSTLRE scheme. To explore the influence of the 3DSTLRE scheme on the accuracy of SAT simulation across the TP, we conducted two numerical experiments. The only difference between the two experiments is that the SEXP (CTRL) experiment is conducted using the RegCM4 with (without) the 3DSTLRE. The terrain correction factors at the grid level reveal that the most intense 3DSTLRE are observed along the periphery of the TP, particularly in the western and southeastern areas (Figures 2a and 2b). The scope of both experiments includes the TP as well as the adjacent areas (Figure 2c). Please refer to Table 1 for the detailed information on the model configuration.

The simulations in both experiments start at 00:00:00 UTC on 1 July 2009, end at 00:00:00 UTC on 1 January 2016, and output the model results every 1 hr. The outputs during the period from 1 January 2010 to 31 December 2015 are used for analysis.

2.4. Data for Model Evaluation

The data used for model evaluation are listed in Table 2. The daily SDLR from the GLASS data set and the hourly SDLR from the TPDC are averaged to the monthly SDLR. Then the monthly SDLR from the CLARA-A2, TPDC, CERES, and GLASS data sets, the monthly total cloud cover from the CLARA-A2 data set, and the hourly SAT from the CLDAS data set are remapped to the model grids of RegCM4. The arithmetic average method is used from high resolution interpolation to low resolution, and bilinear interpolation method is used from low resolution interpolation to high resolution. The ensemble average value of the SDLR from the four data sets is calculated to reduce the uncertainty of the satellite observations and is referred to as the observation (OBS), which is used for the evaluation of the simulated SDLR.

2.5. The Metrics of Model Evaluation

The Root Mean Square Error (RMSE) serves as a metric for evaluating the model's accuracy. A lower RMSE signifies superior model performance. To quantitatively evaluate the results of the numerical experiments, the

21698996, 2024, 23, Downloaded from https://agupubs.onlinelibrary.wiley.com/doi/10.1029/2024JD042102 by Nanjing University, Wiley Online Library on [19/06/2025]. See the Terms and Conditions (https://onlinelibrary.wiley.com/terms-and-conditions) on Wiley Online Library for rules of use; OA articles are governed by the applicable Creative Commons License

21698996, 2024, 23, Downloaded from https://agupubs.onlinelibrary.wiley.com/doi/10.1029/2024JD042102 by Nanjing University, Wiley Online Library on [19/06/2025]. See the Terms and Conditions (https://onlinelibrary.wiley.com/terms-and-conditions) on Wiley Online Library for rules of use; OA articles are governed by the applicable Creative Commons License

Table 1
Model Configuration

Items	Values	Reference
Dynamic core	Hydrostatical core	Grell et al. (1994)
Horizontal grid	Arakawa B-grid Coordinate System 140 (90) grids in the latitude (longitude) direction Horizontal Resolution 30 km Lambert Conformal Projection Model Center (87°E, 33°N)	–
Vertical levels	Sigma Coordinate System 18 Vertical Levels Top at 50 hPa	–
Initial & lateral boundary condition	ERA-Interim Reanalysis of 1.5° NOAA OISST of 1.0° Updated Every 6 Hr	Dee et al. (2011), Reynolds et al. (2002)
Initial soil moisture for shorting spin-up time	Soil moisture from ESA CCI product of 0.25°	Dorigo et al. (2021)
Grid-scale topography	GMTED of 30″	Danielson and Gesch (2011)
Planetary Boundary Layer (PBL) scheme	Holtslag PBL scheme	Holtslag et al. (1990)
Convective scheme	Tiedtke cumulus scheme	Tiedtke (1996)
Radiation transfer module	CCM3 radiation scheme	Kiehl et al. (1998)
Large-scale precipitation scheme	SUBEX scheme	Pal et al. (2000)
Ocean flux scheme	Zeng ocean scheme	Zeng et al. (1998)
Land surface model	Community Land Model V4.5	Oleson et al. (2013)
Integral period	00:00:00 1 July 2009 to 00:00:00 1 January 2016 UTC (Spin-up Period: 1 July 2009–31 December 2009) (Analysis Period: 1 January 2010–31 December 2015)	–
Integral interval	40 Seconds for Dynamic Core 40 Seconds for Cumulus Scheme 20 Minutes for Solar Radiation Calculation 3 Hr for Atmospheric Absorption-emission Calculation 30 Min for Land Surface Model	–
Output interval	1 Hr	–

model domain is divided into two sub-regions. The sub-regions Reg1 and Reg2 (Figure 2a) are the areas with an elevation above 3,000 m in the range of (70–105°E, 26–41°N) and (70–80°E, 30–41°N), respectively. The Reg1 covers the entire TP, while the Reg2 covers the western TP.

3. Impact of the 3DSTLRE Scheme on the SAT Simulation

Figures 3a–3c show that the RegCM4 with or without considering the 3DSTLRE both can reproduce the climatic patterns of the SAT in the TP during 2010–2015. However, in the CTRL experiment, the SAT simulated by the RegCM4 model without the 3DSTLRE shows evident cold bias in the TP and with the intensity more than −5°C located in the western and southeastern TP, where the terrains are much more complex (Figure 3d). The SEXP experiment significantly mitigates the underestimation of SAT in the CTRL experiment across the majority of the TP (Figures 3d and 3e) with the largest reduction located in the western TP. The RMSE for the SAT simulation in the SEXP experiment, is notably decreased in most of the TP and the western part of the TP experiences a more substantial reduction in RMSE, exceeding 9.0% relative to the CTRL experiment (Figure 3f).

Table 2
Data for Evaluation

Data set	Variable	Horizontal resolution	Period/Frequency	Reference
CLARA-A2	SDLR, Total cloud fraction	0.25° × 0.25°	2010–2015/Monthly	Karlsson et al., 2017
GLASS	SDLR	0.05° × 0.05°	2010–2015/Daily	Xu et al., 2022
CERES SYN1deg_Ed4.1	SDLR	1° × 1°	2010–2015/Monthly	Doelling et al., 2016
Machine learning-based SDLR provided by TPDC	SDLR	0.25° × 0.25°	2010–2015/Hourly	Wang et al., 2022
CLDAS	SAT	0.0625° × 0.0625°	2010–2015/Hourly	X. Huang et al. (2022)

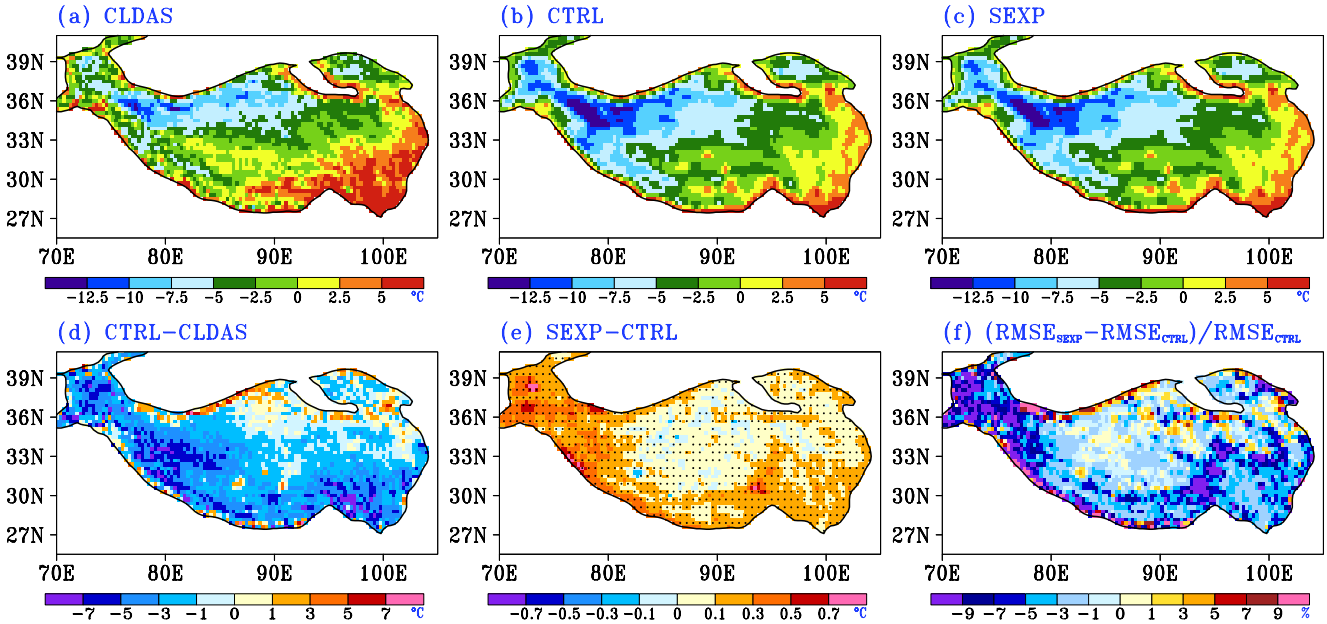

Figure 3. The average SAT for the period 2010–2015, as derived from the CLDAS data set is depicted in (a), while the CTRL simulation is shown in (b) and the SEXP simulation in (c). Panel (d) illustrates the discrepancy in the average SAT between the CTRL simulation and the CLDAS data set, and panel (e) shows the variance between the SEXP and CTRL simulations for the same period. The relative discrepancy in the root mean square error (RMSE) of the modeled SAT for the SEXP versus the CTRL simulation is presented in panel (f) for the 2010–2015 timeframe. The black solid lines in the figures represent the 3,000-m contour. In panel (e), the dots signify the statistical significance of differences at the 95% confidence level according to Student's *t*-test.

Figures 4a–4d show that the cold bias of the simulated daytime SAT in the CTRL experiment is situated across almost the entire TP in winter and spring, and in the western and southern part of the TP during summer and autumn. Compared to the CTRL experiment, the SEXP experiment produced much higher daytime SAT in the majority of TP during winter and spring and in the western TP during summer and autumn (Figures 4e–4h). These differences can reduce the cold bias produced by the CTRL experiment to a certain extent. The proportional variations in the RMSE of the simulated SAT in the TP further indicate that the inclusion of the 3DSTLRE can clearly improve the simulations of SAT across most of the TP in winter and spring, as well as in the western TP during summer and autumn (Figures 4i–4l). The outcomes at nighttime are akin to those during the daytime, but the improvement of SAT simulations induced by the adoption of 3DSTLRE is more evident at nighttime (Figures 4i–4l and 4u-4x).

Figure 5 illustrates that the 3DSTLRE scheme effectively diminishes the RMSE of the modeled SAT across both daytime and nighttime in different seasons over the sub-regions Reg1 and Reg2. Compared to the CTRL experiment without 3DSTLRE, the SEXP experiment with the 3DSTLRE results in a reduction of the RMSE for the simulation of SAT over sub-region Reg1 at daytime (nighttime) by 3.0%, 1.7%, 1.7%, and 2.4% (4.4%, 3.4%, 2.5%, and 2.6%) during winter, spring, summer, and autumn, respectively (Figures 5e and 5f). The improvement of the simulated SAT induced by the adoption of 3DSTLRE scheme is more evident over the sub-region Reg2 than over the sub-region Reg1. From Figures 5g and 5h, the inclusion of the 3DSTLRE can lead to a reduction in the RMSE of the simulated SAT in the sub-region Reg2, with the RMSE of simulated SAT at daytime (nighttime) reduced by 5.3%, 3.2%, 4.4%, and 6.5% (5.6%, 6.0%, 6.1%, and 8.4%) during winter, spring, summer, and autumn, respectively. Overall, the improvement of the simulated SAT induced by the 3DSTLRE over the both sub-regions is more evident in nighttime than in daytime.

4. Physical Mechanisms

Figures 6a–6c display the distributions of the SDLR flux averaged over 2010–2015 from the OBS data and model simulations. The observed SDLR decreases from the southeastern to the northwestern parts of the TP. Both experiments can reproduce the overall spatial pattern of SDLR in the TP (Figures 6b and 6c). The CTRL experiment without the 3DSTLRE substantially underestimates the SDLR over the majority of the TP. This

21698996, 2024, 23, Downloaded from https://agupubs.onlinelibrary.wiley.com/doi/10.1029/2024JD042102 by Nanjing University, Wiley Online Library on [19/06/2025]. See the Terms and Conditions (https://onlinelibrary.wiley.com/terms-and-conditions) on Wiley Online Library for rules of use; OA articles are governed by the applicable Creative Commons License

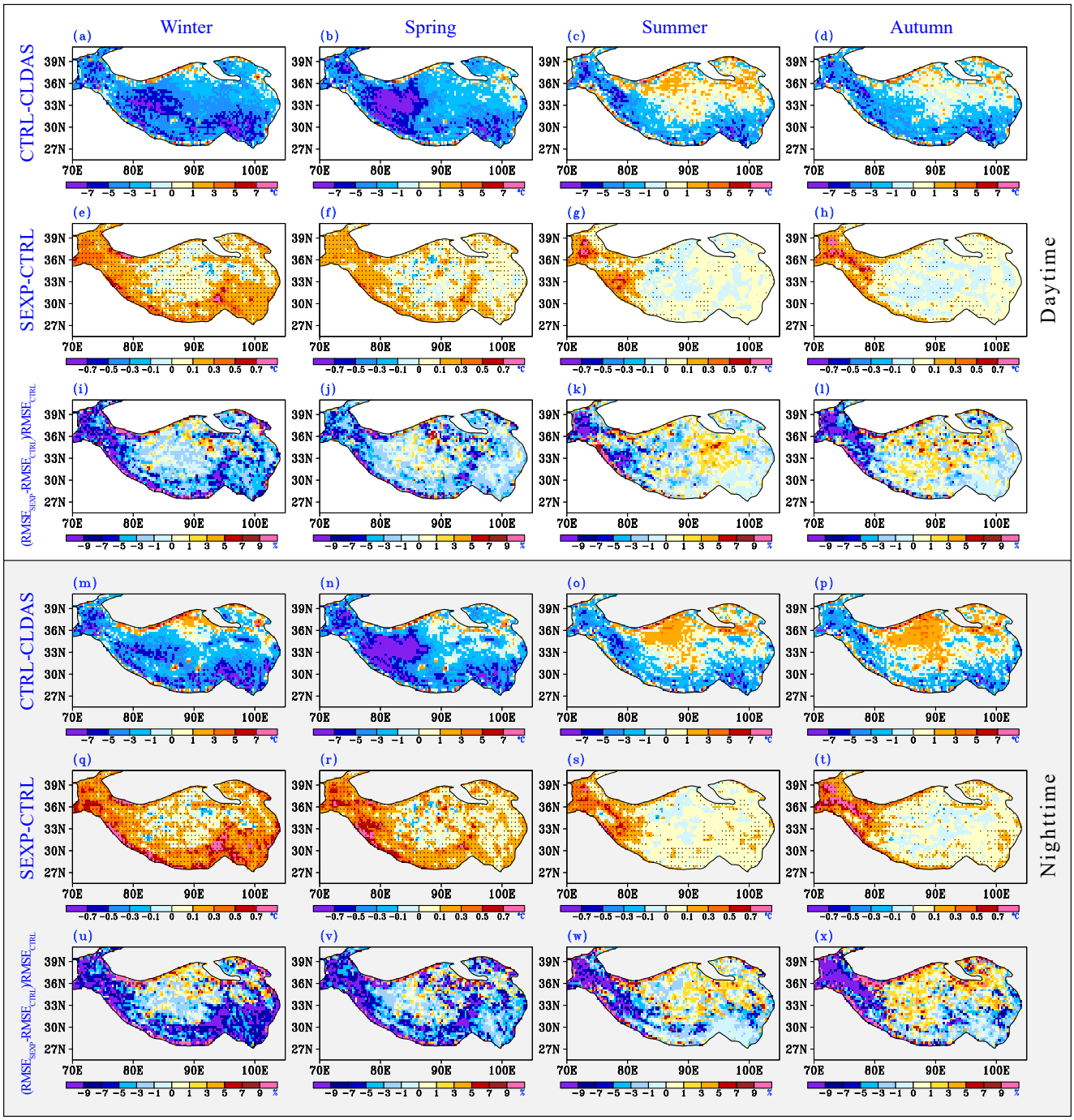

Figure 4. The differences of the climatic mean SAT over 2010–2015 between the CTRL simulations and the CLDAS data set (a–d, m–p), and between both simulations (e–h, q–t), and the relative variation in the RMSE of the simulated SAT between both experiments (i–l, u–x) during the daytime (a–l) and nighttime (m–x) in different seasons over 2010–2015. The dots in panels (e–h and q–t) indicate the differences exceeding the 95% confidence threshold as determined by Student's *t*-test.

underestimation is notably pronounced, with values exceeding −20 W·m^{-2}, particularly along the northwestern and southern boundaries of the plateau (Figure 6d). The SEXP experiment with the 3DSTLRE notably improves the simulated SDLR across much of the TP, particularly at the southern edges where the terrain is complex, the increase in SDLR is significantly obvious with an increment of 15 W·m^{-2} relative to the CTRL experiment (Figure 6e). The enhancement in SDLR could be predominantly ascribed to the longwave radiation flux emitted from the surrounding topographies. The RMSE of the SDLR simulated by the SEXP experiment is clearly

21698996, 2024, 23, Downloaded from https://agupubs.onlinelibrary.wiley.com/doi/10.1029/2024JD042102 by Nanjing University, Wiley Online Library on [19/06/2025]. See the Terms and Conditions (https://onlinelibrary.wiley.com/terms-and-conditions) on Wiley Online Library for rules of use; OA articles are governed by the applicable Creative Commons License

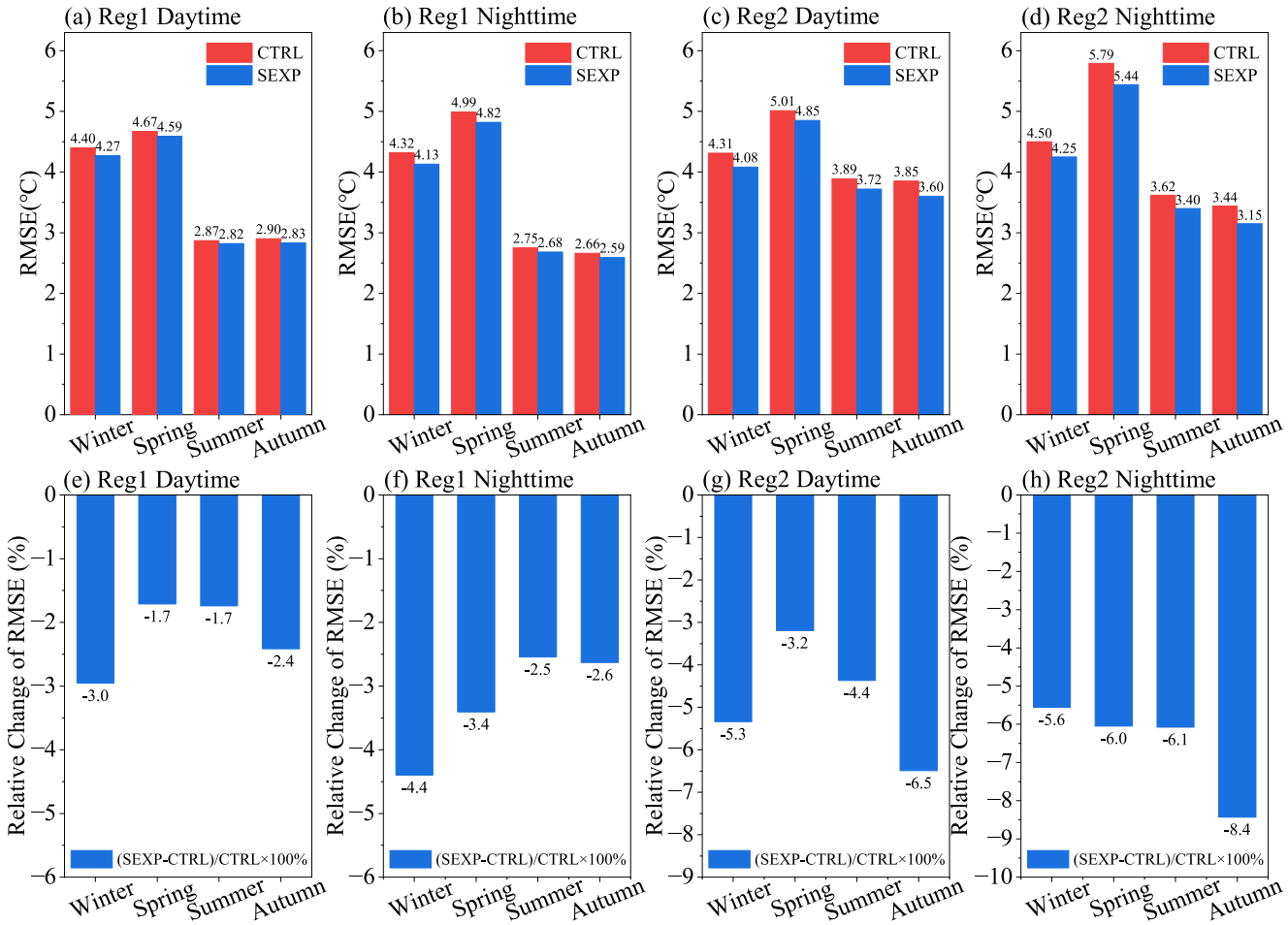

Figure 5. The regional averages of the RMSE for the SAT simulations between the both experiments are presented for the years 2010–2015, categorized by daytime and nighttime across various seasons in two sub-regions (a–d). These sub-regions, defined by elevations exceeding 3,000 m, correspond to the red (Reg1) and black (Reg2) rectangles depicted in Figure 2a. Additionally, the relative shifts in RMSE are detailed in (e–h).

reduced in most of the TP compared to the CTRL experiment (Figure 6f). The RMSE of the SDLR simulated by the SEXP experiment experiences a reduction exceeding 40% at the majority of the TP's peripheries relative to the CTRL experiment, suggesting that the inclusion of the 3DSTLRE can significantly enhances the accuracy of SDLR simulations over the complex and rugged terrains.

Figures 6g–6j demonstrate that RegCM4 significantly underestimates the total cloud cover over the TP, with the underestimation exceeding 20%. After adopting the 3DSTLRE scheme, the total cloud cover simulated by the SEXP experiment shows a slight increase compared to the CTRL experiment (Figure 6k). This increase is primarily attributed to the rise in surface air temperature and the resulting atmospheric thermal feedback. Notably, the increase in cloud cover is concentrated over the elevated regions of the TP, where the RMSE of the simulated total cloud cover has decreased by more than 2% (Figure 6l). It is important to note that the improvement in the simulation of total cloud cover by the 3DSTLRE scheme is minimal. The limited capability in cloud simulation is a significant source of SDLR errors in the RegCM4's simulation of the TP. Therefore, enhancing the cloud simulation performance of RegCM4 is essential.

Relative to the CTRL experiment, the RMSE of the SDLR in sub-region Reg1 (Reg2) simulated by the SEXP experiment is reduced by 20.4%, 18.2%, 18.5%, and 22.6% (6.7%, 29.5%, 33.6%, and 36.3%) during winter, spring, summer, and autumn, respectively (Figures 7c and 7d). Overall, the implementation of the 3DSTLRE scheme undoubtedly enhances the RegCM4 model's capability to simulate SDLR in the rugged terrains.

21698996, 2024, 23, Downloaded from https://agupubs.onlinelibrary.wiley.com/doi/10.1029/2024JD042102 by Nanjing University, Wiley Online Library on [19/06/2025]. See the Terms and Conditions (https://onlinelibrary.wiley.com/terms-and-conditions) on Wiley Online Library for rules of use; OA articles are governed by the applicable Creative Commons License

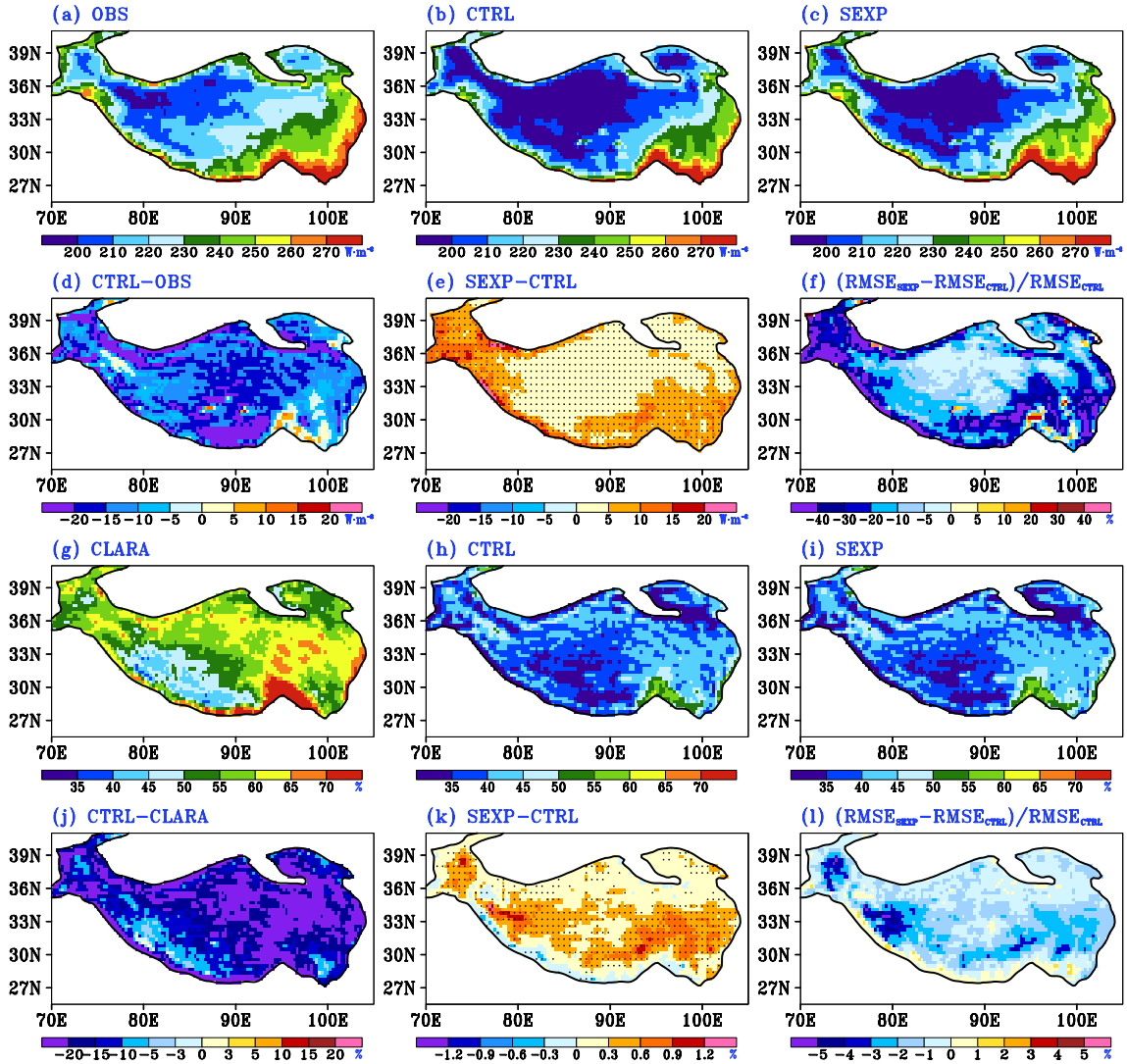

Figure 6. The average SDLR and total cloud cover for the period 2010–2015 is depicted from observational data (OBS data set and CLARA data set) in (a, g), the CTRL simulation in (b, h), and the SEXP simulation in (c, i). The discrepancies in average SDLR (total cloud cover) between the CTRL simulation and OBS (CLARA) data set are shown in panels (d, j), and between both simulations in panels (e, k). Additionally, panels (f, l) illustrates the relative changes in the RMSE of the SDLR and total cloud cover as simulated by the modified RegCM4 with the 3DSTLRE compared to the CTRL over the 2010–2015 period. The black solid lines in the figures represent the 3,000-m altitude contour. In panels (e, k), the dots highlight the areas where the differences are statistically significant at the 95% confidence level, as determined by Student's *t*-test.

In this study, the surface net radiation (SNR), surface net solar radiation (SNSR), SDLR, and surface downward solar radiation (SDSR) are all positive downward. Conversely, surface latent heat (LH) flux, surface net longwave radiation (SNLR), and surface sensible heat (SH) flux are positive upward. Figure 8 shows the disparities in the modeled surface radiation components between the two experiments. The SDLR simulated by the SEXP experiment surpasses that of the CTRL experiment by more than 15 W·m^{-2} in the TP during daytime hours (Figures 8a1–8a4). The daytime SULR simulated by the SEXP experiment exhibits a modest rise relative to the CTRL experiment (not shown), this can be attributed to the increase in ground surface temperature. Therefore, the reduced daytime SNLR in the SEXP experiment mainly resulted from the increased SDLR (Figures 8a1–8b4). The variations in the modeled SDSR between the two experiments are relatively minor (Figures 8c1–8c4). The modest decrease in SDSR found in the SEXP experiment is a result of the heightened cloud cover (Figure 6k). The increased SNSR in the SEXP experiment (Figures 8d1–8d4) should be attributed to the reduced surface albedo, which is the feedback of the increased surface temperature (not shown). In all, the increased daytime SNR during different seasons in the SEXP experiment (Figures 8e1–8e4) is mainly attributed to the increased SDLR, which is

21698996, 2024, 23, Downloaded from https://agupubs.onlinelibrary.wiley.com/doi/10.1029/2024JD042102 by Nanjing University, Wiley Online Library on [19/06/2025]. See the Terms and Conditions (https://onlinelibrary.wiley.com/terms-and-conditions) on Wiley Online Library for rules of use; OA articles are governed by the applicable Creative Commons License

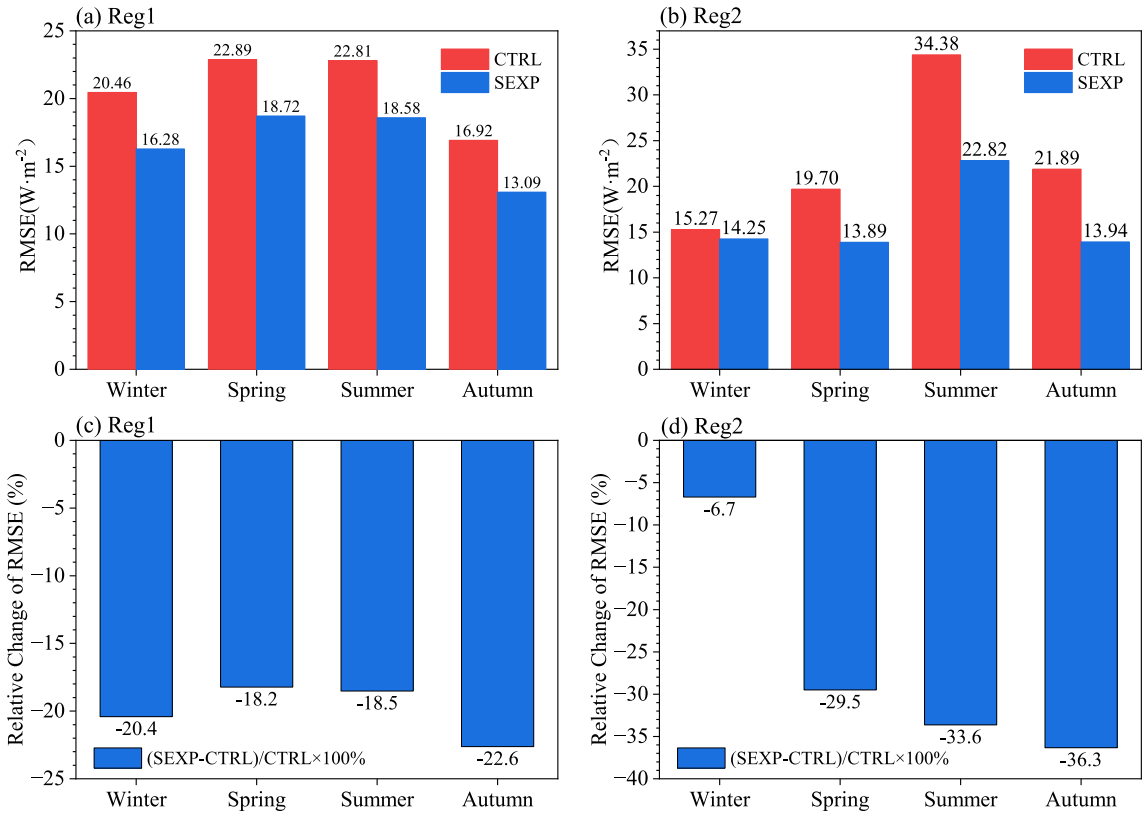

Figure 7. The regionally averaged RMSE of the simulated surface downward longwave radiation (SDLR) over 2010–2015 in both experiments across sub-regions Reg1 and Reg2 in different seasons (a, b) and its relative changes (c, d). The sub-regions Reg1 and Reg2 are the areas above 3,000 m in the red and blue rectangles shown in Figure 2a, respectively.

resulted from the direct impact of the 3DSTLRE scheme. Similar to daytime, the increased SNR at nighttime during different seasons in the SEXP experiment mainly results from the enhanced SDLR induced by the 3DSTLRE relative to CTRL experiment (Figures 8f1–8h4).

Figure 9 provides a detailed comparison of the differences in SH, LH, and the combined surface sensible and latent heat (SHLH) flux between the two experiments. The differences in the modeled SHLH, predominantly driven by SH, are on par with the discrepancies in the SNR between the two experiments (Figures 8e1–8e4, 8h1–8h4, 9c1–9c4, and 9f1–9f4), implying that the majority of the increased SDLR induced by the 3DSTLRE scheme is primarily transformed into SH, which in turn directly warms the surface air and leads to the increase of SAT.

Figure 10 presents the regional mean differences of surface energy components between the two experiments in the sub-regions Reg1 and Reg2. The differences in the SNR show comparable magnitudes to those of the SNLR in the sub-regions Reg1 and Reg2 during daytime and nighttime throughout a year (Figures 10a–10d), indicating that the indirect feedback from the land surface and atmosphere, such as reduced surface albedo and increased solar irradiance due to reduced cloud cover, is not the primary reasons for the improvement of the simulated SAT. Figure 10 also indicates that the increased SNR induced by the 3DSTLRE in different seasons predominantly contributes to the increases of SH flux, which directly warm the near surface air. Although the increased SDLR and SNR due to the 3DSTLRE is much larger in daytime than in nighttime (Figures 10e−10h), the SAT increases more at nighttime than at daytime (Figures 4e–4h and 4q–4t), this should be attributed to the diurnal boundary layer differences.

Figure 11 illustrates the diurnal variation of the differences in the simulated SH and SAT between the two experiments, as well as the diurnal variation of the boundary layer height from the two experiments. The maximum differences of the simulated SH are observed in the afternoon, whereas the maximum differences in the simulated

21698996, 2024, 23, Downloaded from https://agupubs.onlinelibrary.wiley.com/doi/10.1029/2024JD042102 by Nanjing University, Wiley Online Library on [19/06/2025]. See the Terms and Conditions (https://onlinelibrary.wiley.com/terms-and-conditions) on Wiley Online Library for rules of use; OA articles are governed by the applicable Creative Commons License

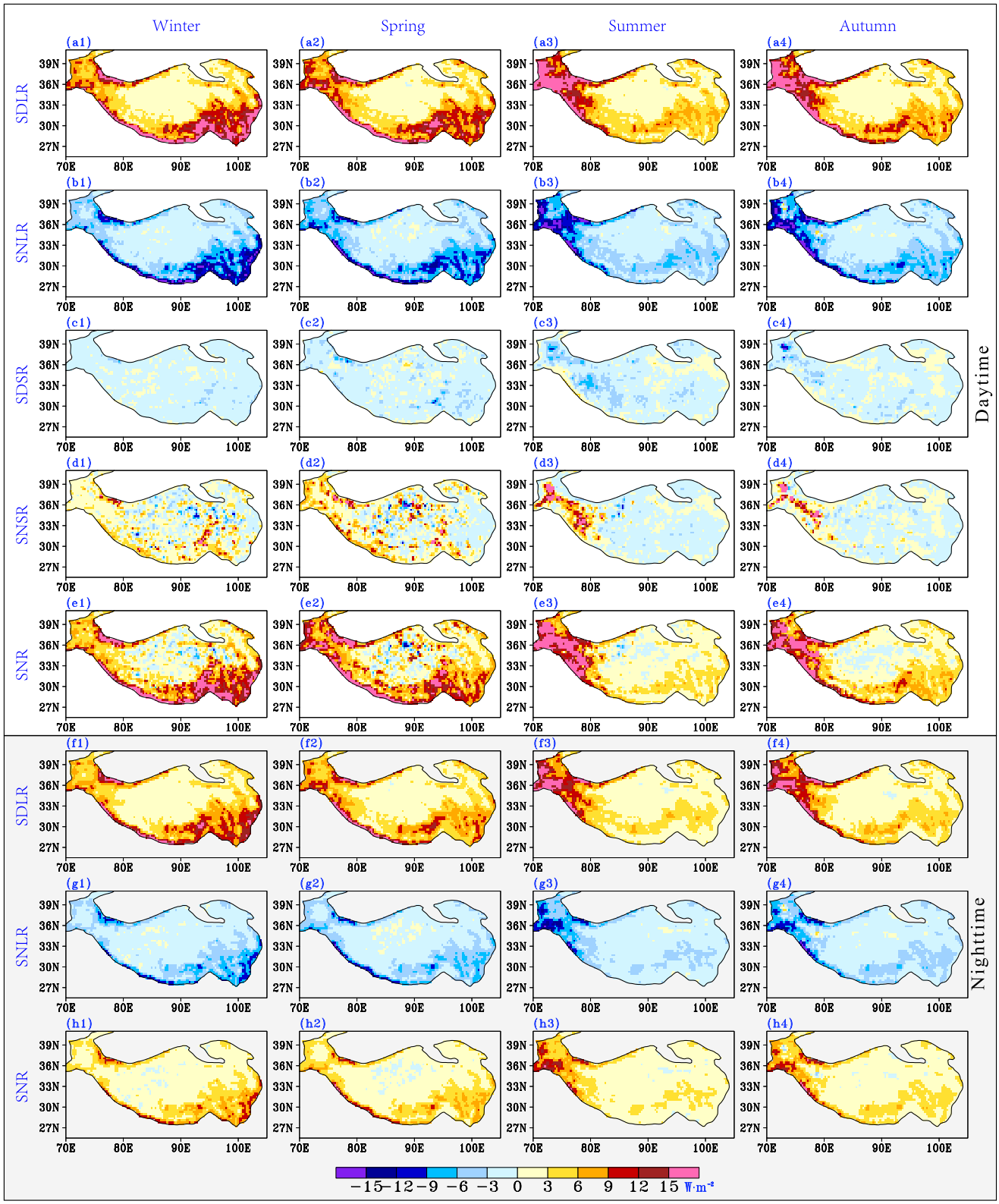

Figure 8. The disparities in the modeled variables—surface downward longwave radiation (SDLR) in panels a1–a4 and f1–f4, surface net longwave radiation (SNLR) in panels b1–b4 and g1–g4, surface downward solar radiation (SDSR) in panels c1-c4, surface net solar radiation (SNSR) in panels d1–d4, and surface net radiation (SNR) in panels e1–e4 and h1–h4 are illustrated between both experiments across different seasons for the period 2010–2015. Panels a1–e4 represent the daytime averages, whereas panels f1–h4 depict the nighttime averages.

21698996, 2024, 23, Downloaded from https://agupubs.onlinelibrary.wiley.com/doi/10.1029/2024JD042102 by Nanjing University, Wiley Online Library on [19/06/2025]. See the Terms and Conditions (https://onlinelibrary.wiley.com/terms-and-conditions) on Wiley Online Library for rules of use; OA articles are governed by the applicable Creative Commons License

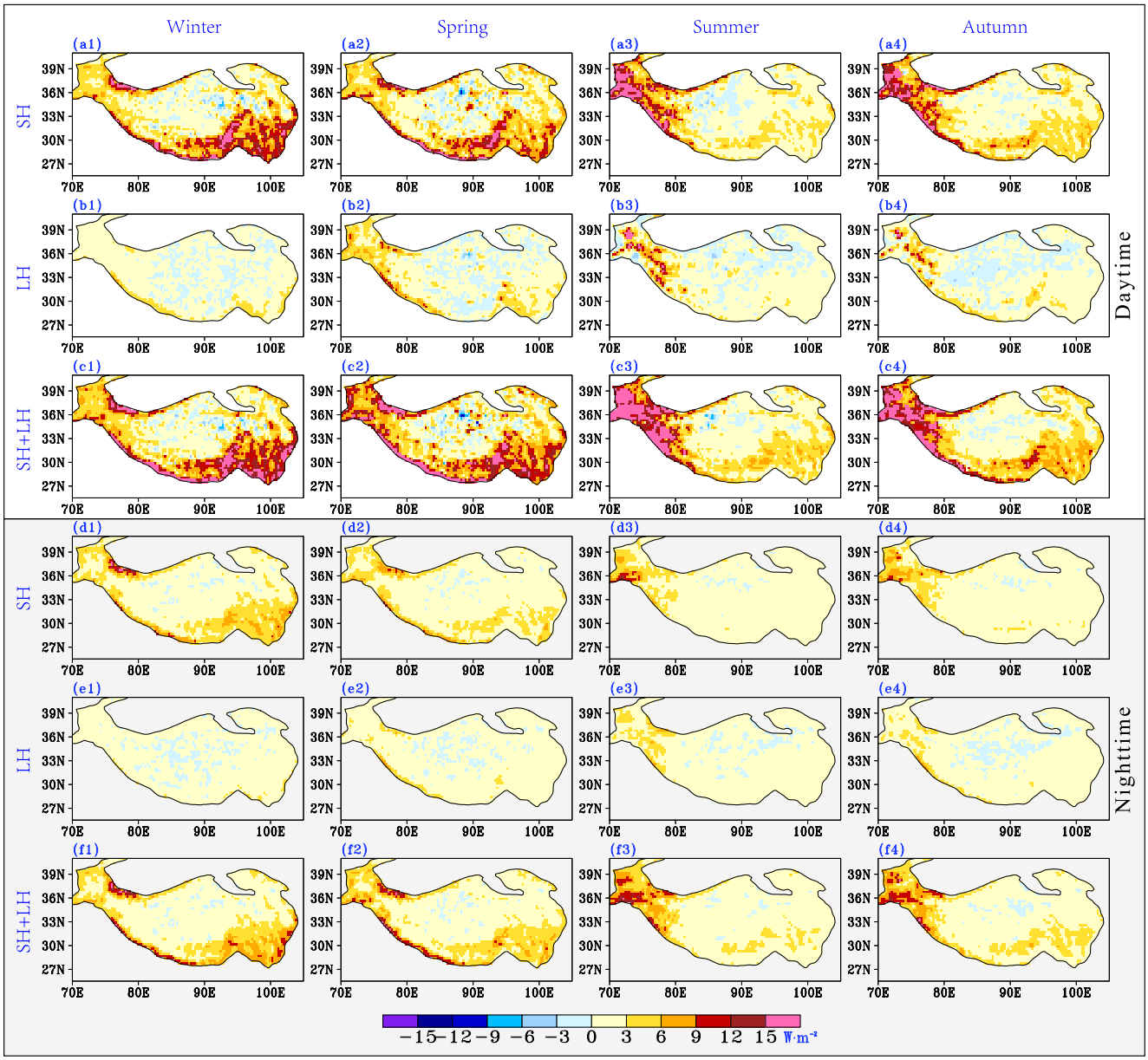

Figure 9. The variations in the calculated surface sensible heat flux (SH) as indicated in panels (a1–a4) and (d1–d4), surface latent heat flux (LH) in panels (b1–b4) and (e1–e4), and the combined total of sensible and latent heat flux (SH + LH) in panels (c1–c4) and (f1–f4) are presented as comparative analyses between both simulations across various seasons for the timeframe of 2010–2015. The daytime averages are depicted in panels (a1–c4), and the nighttime averages are shown in panels (d1–f4).

SAT are noted just before midnight. The diurnal variation of the differences in boundary layer height from both experiments aligns with the diurnal variation in sensible heat flux differences between the two experiments. The SH changes induced by the 3DSTLRE are significantly greater during daytime than during nighttime. However, the increased SH during the daytime necessitates heating a much deeper boundary layer of the atmosphere compared to nighttime. Consequently, the increase in SAT during daytime is not as pronounced as it is in nighttime.

Overall, the RegCM4 underestimates the SDLR over most of the TP with complex sub-grid terrains when the 3DSTLRE is absent. Inclusion of the 3DSTLRE can clearly improve the SDLR simulations over the rugged terrains of TP. Although the SDSR, SUSR, and SULR vary in response to the variation of SDLR induced by the

21698996, 2024, 23, Downloaded from https://agupubs.onlinelibrary.wiley.com/doi/10.1029/2024JD042102 by Nanjing University, Wiley Online Library on [19/06/2025]. See the Terms and Conditions (https://onlinelibrary.wiley.com/terms-and-conditions) on Wiley Online Library for rules of use; OA articles are governed by the applicable Creative Commons License

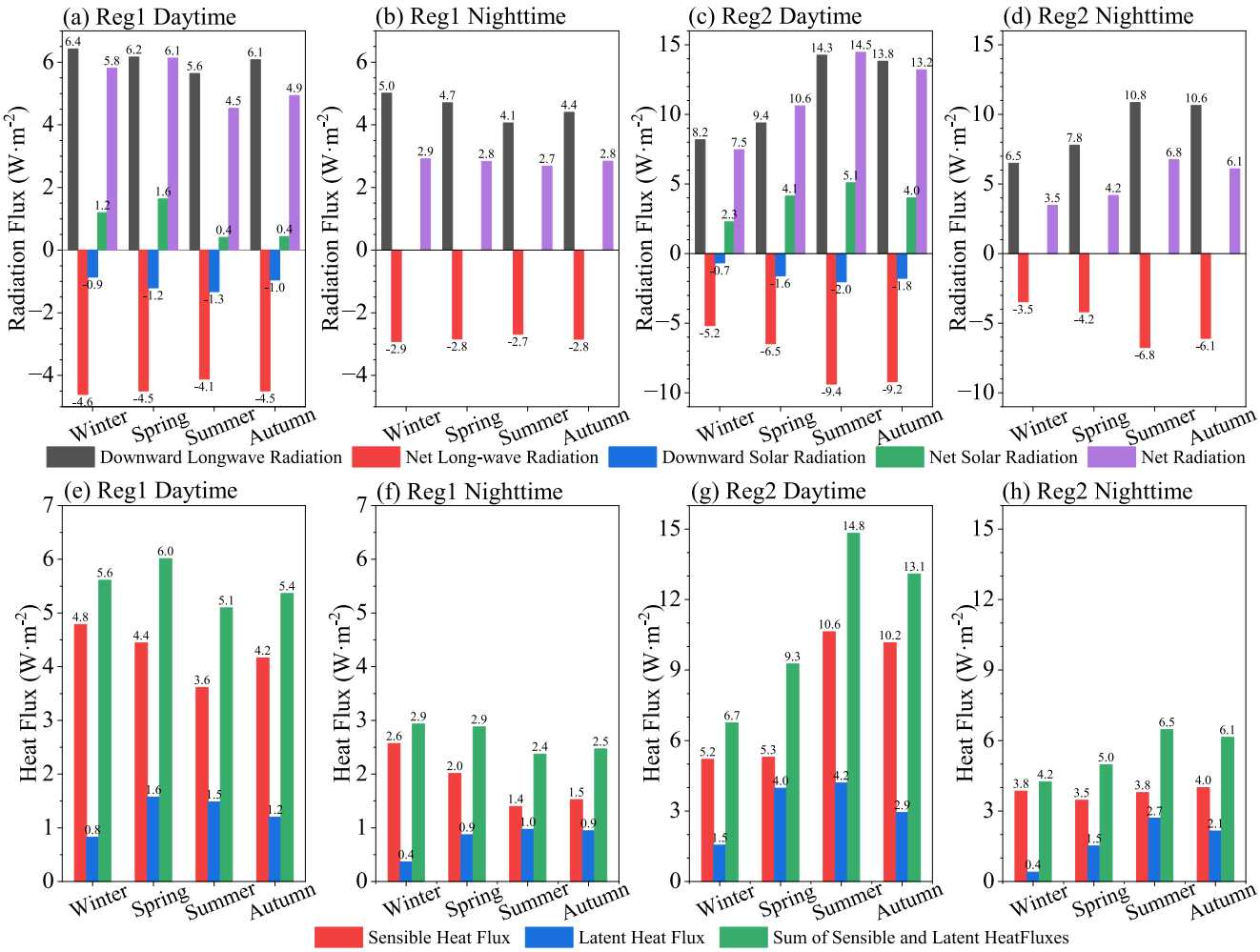

Figure 10. The average regional differences in the modeled surface energy fluxes between the two experiments for sub-regions Reg1 and Reg2 throughout the seasons of 2010–2015. The comparison is depicted for daytime conditions in subplots (a, c, e, g) and for nighttime conditions in subplots (b, d, f, h), with each set of subplots corresponding to a specific season.

3DSTLRE, the main source of the variation in the SHLH flux heating near-surface atmosphere is the change in SDLR. Therefore, the change in the SAT is a direct response to the 3DSTLRE.

5. Conclusion and Discussion

Rugged terrains significantly affect the SDLR, however, the 3DSTLRE are not accounted for in most numerical models. In this study, to assess the influence of 3DSTSRE on the simulation of SDLR and SAT over the TP, we modified the RegCM4 by incorporating the 3DSTLRE scheme and conducted experiments using both the modified and original RegCM4. The key findings are summarized below:

The RegCM4 without 3DSTLRE evidently underestimates the SAT in the TP. The largest underestimation of the annual mean SAT occurs over the western and southern TP with the intensity below −5°C. Inclusion of the 3DSTLRE can lead to the simulated annual mean SAT increased by more than 0.7°C. The RMSE of the simulated SAT over the western TP can be reduced by more than 9.0% due to the adoption of the 3DSTLRE scheme. Compared to the CTRL experiment, the RMSE of the daytime (nighttime) SAT across the entire TP region simulated by the experiment SEXP with the 3DSTLRE is decreased by 3.0%, 1.7%, 1.7%, and 2.4% (4.4%, 3.4%, 2.5%, and 2.6%) in winter, spring, summer, and autumn, respectively. Over the western TP with much more

21698996, 2024, 23, Downloaded from https://agupubs.onlinelibrary.wiley.com/doi/10.1029/2024JD042102 by Nanjing University, Wiley Online Library on [19/06/2025]. See the Terms and Conditions (https://onlinelibrary.wiley.com/terms-and-conditions) on Wiley Online Library for rules of use; OA articles are governed by the applicable Creative Commons License

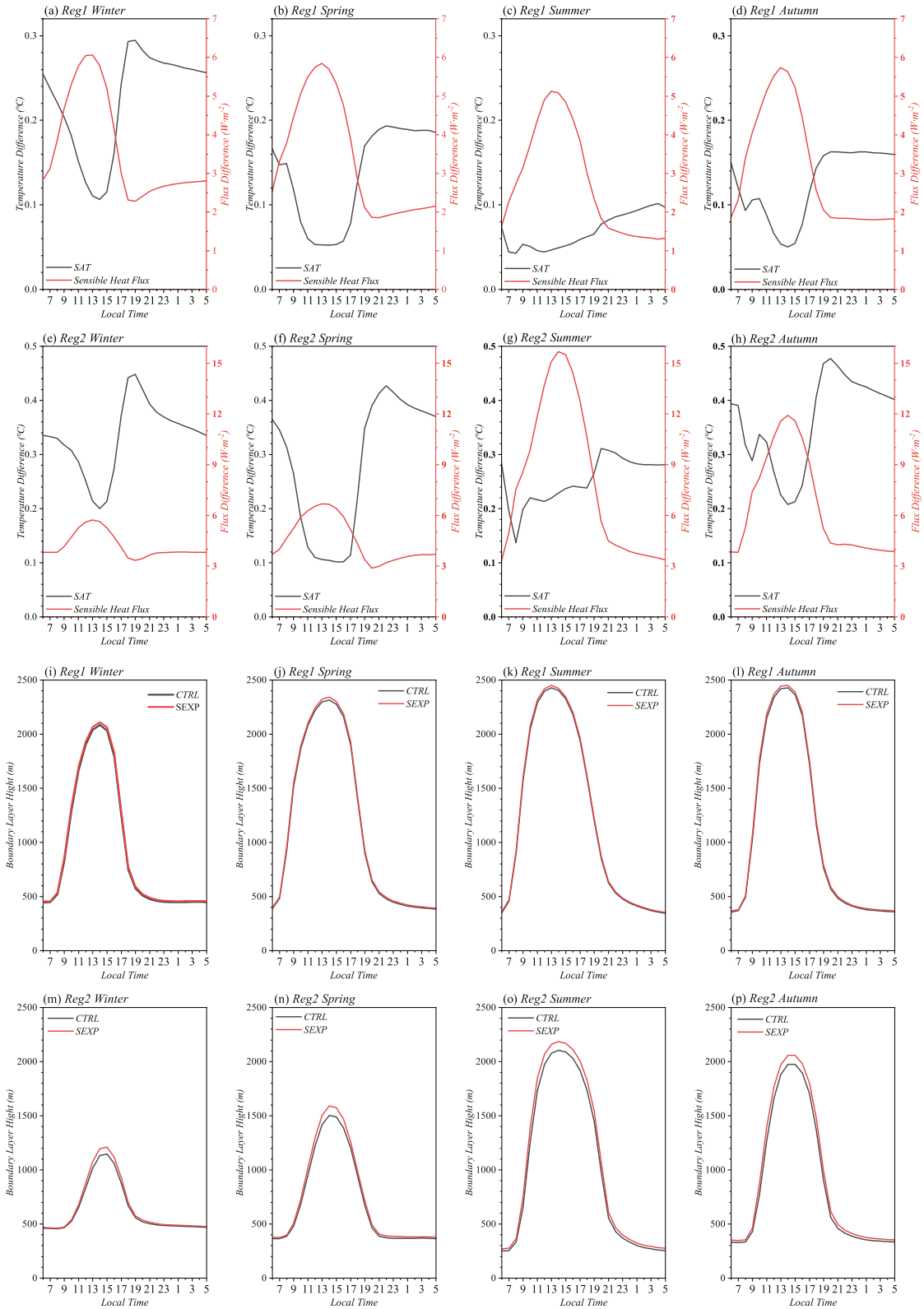

Figure 11. The diurnal variation of the regional mean differences of the modeled SAT and sensible heat flux between the two experiments are showcased for sub-regions Reg1 in panels (a, b, e, f) and Reg2 in panels (c, d, g, h) across various seasons from 2010 to 2015, as well as, the diurnal variation of the regional mean of the modeled boundary layer height in the two experiments are shown for sub-regions Reg1 in panels (i, j, k, l) and Reg2 in panels (m, n, o, p) across various seasons from 2010 to 2015.

21698996, 2024, 23, Downloaded from https://agupubs.onlinelibrary.wiley.com/doi/10.1029/2024JD042102 by Nanjing University, Wiley Online Library on [19/06/2025]. See the Terms and Conditions (https://onlinelibrary.wiley.com/terms-and-conditions) on Wiley Online Library for rules of use; OA articles are governed by the applicable Creative Commons License

21698996, 2024, 23, Downloaded from https://agupubs.onlinelibrary.wiley.com/doi/10.1029/2024JD042102 by Nanjing University, Wiley Online Library on [19/06/2025]. See the Terms and Conditions (https://onlinelibrary.wiley.com/terms-and-conditions) on Wiley Online Library for rules of use; OA articles are governed by the applicable Creative Commons License

complex sub-grid terrains, the improvement of the SAT simulations induced by the 3DSTLRE is more evident than that over the entire TP. Adopting the 3DSTLRE scheme can lead to the RMSE of the simulated SAT in the western TP reduced by 5.3%, 3.2%, 4.4%, and 6.5% (5.6%, 6.0%, 6.0%, and 8.4%) during daytime (nighttime) in the winter, spring, summer, and autumn, respectively. Overall, the improvements of the SAT simulation in both the western TP and the entire TP induced by the 3DSTLRE scheme are slightly more noticeable in nighttime than in daytime.

The improvement of the SAT simulation is primarily a direct response to the improvement of SDLR simulation. The RegCM4 without the 3DSTLRE significantly underestimates the SDLR over the TP by more than -20 W·m^{-2}, and the underestimation is more pronounced at the edges of TP with rugged terrains. Considering of the 3DSTLRE can evidently reduce the underestimation of the SDLR over the TP. Inclusion of the 3DSTLRE in the SEXP experiment can lead to the RMSE of the SDLR simulated by the CTRL experiment without the 3DSTLRE reduced by 20.4%, 18.2%, 18.5%, and 22.6% (6.7%, 29.5%, 33.6%, and 36.3%) over the entire TP (the western TP) in the winter, spring, summer, and autumn, respectively.

Most of the increased SDLR induced by the 3DSTLRE mainly leads to the sensible heat flux increased, which further warms the near surface air and thereafter increases the SAT. The alterations in surface upward longwave radiation and solar radiation at the surface, which are a consequence of the land surface and atmospheric response to the 3DSTLRE, exert negligible effects on the modeled SAT. Due to the diurnal boundary layer difference, the increase of the SAT is more pronounced in nighttime than during daytime.

Although the simulation of the SDLR and SAT in the rugged areas of TP can be improved by the inclusion of the 3DSTLRE scheme in the RegCM4 model to some extent, noticeable cold biases and underestimation of the SDLR still persist. According to previous studies (An et al., 2022; Lee, Li et al., 2019; Wang et al., 2023; X. Zhou et al., 2023), we believe that efforts should be made to improve the description of snow, surface albedo, and atmospheric radiative transfer in the RegCM4 model, which may improve the simulation of the SAT. The simulation of clouds by RegCM4 contains significant errors that greatly affect SDLR simulations. Therefore, it is essential to focus on enhancing the accuracy of cloud simulations (Pareja-Quispe et al., 2021).

Additionally, further work is essential to investigate how the combinations of sub-grid terrain long-wave and solar radiation effects affect the performance of the RegCM4 model in simulating the climate of the TP and its surrounding areas. The experiments conducted in this study do not utilize the optimal model configurations, including low horizontal and vertical resolutions, the implementation of imperfect schemes such as SUBEX, and the reliance on ERA-Interim forcing fields. It is essential to further evaluate the effectiveness of the 3DSTLRE scheme by employing various model configurations over the different regions with rugged terrain.

Data Availability Statement

Data—The SRTM elevation data (Jarvis et al., 2008), the GMTED elevation data (Danielson & Gesch, 2011), the NOAA OISST data (NOAA, 2002; Reynolds et al., 2002), the ERA-Interim reanalysis (Dee et al., 2011; ECMWF, 2011), the ESA CCI ECV soil moisture data (ESA, 2012; Liu et al., 2012), the CLARA-A2.1 SDLR data (Karlsson et al., 2020), the GLASS SDLR data (NESSDC, 2022); the SDLR provided by TPDC (Wang & Wang, 2022), the SAT from the CLDAS data set (CMDC, 2019; Han et al., 2019), and the SDLR from the CERES SYN1deg_Ed4.1 data sets (Doelling et al., 2016; NASA, 2016). Software—The source codes for the original and modified RegCM4 (Gu & Huang, 2024).

Acknowledgments
This study is supported by the National Natural Science Foundation of China under Grant 42375157, the National Key R&D Program of China under Grant 2022YFC3080500, the Beijige Research Fund of NJIAS (BJG202403), the CAS "Light of West China" Program (E129030101), Open Research Fund Program of Plateau Atmosphere and Environment Key Laboratory of Sichuan Province (PAEKL-2023-K01), the Research Funds for the Frontiers Science Center for Critical Earth Material Cycling Nanjing University, the Fundamental Research Funds for the Central Universities (020914380103), the Jiangsu University "Blue Project" outstanding young teachers training object, and the Jiangsu Collaborative Innovation Center for Climate Change. Both High Performance Computing Center of Nanjing University, and National Key Scientific and Technological Infrastructure project "Earth System Numerical Simulation Facility" (EarthLab) offer computational resource. We appreciate the various agencies for providing us with data and models. We sincerely thank the two anonymous reviewers and the editor for their help.

References

Abish, B., & Arun, K. (2019). Resolving the weakening of orographic rainfall over India using a regional climate model RegCM 4.5. *Atmospheric Research*, *227*, 125–139. https://doi.org/10.1016/j.atmosres.2019.05.003

An, Y., Meng, X., Zhao, L., Li, Z., Wang, S., Shang, L., et al. (2022). Evaluation of surface albedo over the Tibetan Plateau simulated by CMIP5 models using in-situ measurements and MODIS. *International Journal of Climatology*, *42*(2), 928–951. https://doi.org/10.1002/joc.7281

Arnold, N. S., Rees, W. G., Hodson, A. J., & Kohler, J. (2006). Topographic controls on the surface energy balance of a high Arctic valley glacier. *Journal of Geophysical Research*, *111*(F2). https://doi.org/10.1029/2005jf000426

Arthur, R. S., Lundquist, K. A., Mirocha, J. D., & Chow, F. K. (2018). Topographic effects on radiation in the WRF model with the Immersed boundary method: Implementation, validation, and application to complex terrain. *Monthly Weather Review*, *146*(10), 3277–3292. https://doi.org/10.1175/mwr-d-18-0108.1

Aubry-Wake, C., ZÉPhir, D., Baraer, M., McKenzie, J. M., & Mark, B. G. (2018). Importance of longwave emissions from adjacent terrain on patterns of tropical glacier melt and recession. *Journal of Glaciology*, *64*(243), 49–60. https://doi.org/10.1017/jog.2017.85

Chen, X., Liu, Y., & Wu, G. (2017). Understanding the surface temperature cold bias in CMIP5 AGCMs over the Tibetan Plateau. *Advances in Atmospheric Sciences*, *34*(12), 1447–1460. https://doi.org/10.1007/s00376-017-6326-9

CMDC. (2019). The hourly surface air temperature from China meteorological Administration Land Data Assimilation System (CLDAS) with a horizontal of 0.0625 [Dataset]. *China Meteorological Data Service Center (CMDC)*. Retrieved from http://data.cma.cn/data/cdcdetail/dataCode/NAFP_CLDAS2.0_NRT

Colette, A., Chow, F. K., & Street, R. L. (2003). A numerical study of inversion-layer breakup and the effects of topographic shading in idealized valleys. *Journal of Applied Meteorology*, *42*(9), 1255–1272. https://doi.org/10.1175/1520-0450(2003)042<1255:Ansoib>2.0.Co;2

Coppola, E., Giorgi, F., Giuliani, G., Pichelli, E., Ciarlo, J., Raffaele, F., et al. (2024). The fifth generation regional climate modeling system, RegCM5: The first CP European wide simulation and validation over the CORDEX-CORE domains. *Preprint. ESS Open Archive, January 16, 2024*. https://doi.org/10.22541/essoar.170542078.80092084/v1

Danielson, J. J., & Gesch, D. B. (2011). Global multi-resolution terrain elevation data 2010 (GMTED2010) [Datasets]. *USGS Science for a Changing World*. Retrieved from https://www.usgs.gov/coastal-changes-and-impacts/gmted2010

Dee, D. P., Uppala, S. M., Simmons, A. J., Berrisford, P., Poli, P., Kobayashi, S., et al. (2011). The ERA-interim reanalysis: Configuration and performance of the data assimilation system. *Quarterly Journal of the Royal Meteorological Society*, *137*(656), 553–597. https://doi.org/10.1002/qj.828

Diallo, I., Xue, Y., Chen, Q., Ren, X., & Guo, W. (2022). Effects of spring Tibetan Plateau land temperature anomalies on early summer floods/droughts over the monsoon regions of South East Asia. *Climate Dynamics*, *62*(4), 2659–2681. https://doi.org/10.1007/s00382-021-06053-8

Doelling, D. R., Sun, M., Le, T. N., Nordeen, M. L., & Mlynczak, P. E. (2016). Advances in geostationary-derived longwave fluxes for the Ceres synoptic (Syn1deg) product. *Journal of Atmospheric and Oceanic Technology*, *33*(3), 160118113337004. https://doi.org/10.1175/JTECH-D-15-0147.1

Dorigo, W., Preimesberger, W., Moesinger, L., Pasik, A., Scanlon, T., Hahn, S., et al. (2021). ESA Soil Moisture Climate Change Initiative (Soil_Moisture_cci): COMBINED product, version 06.1 [Datasets]. *NERC EDS Centre for Environmental Data Analysis*. Retrieved from https://catalogue.ceda.ac.uk/uuid/43d73291472444e6b9c2d2420dbad7d6

Dozier, J., & Outcalt, S. (1979). An approach toward energy balance simulation over rugged terrain. *Geographical Analysis*, *11*(1), 65–85. https://doi.org/10.1111/j.1538-4632.1979.tb00673.x

Duguay, C. R. (1995). An approach to the estimation of surface net radiation in mountain areas using remote sensing and digital terrain data. *Theoretical and Applied Climatology*, *52*(1), 55–68. https://doi.org/10.1007/BF00865507

ECMWF. (2011). The hourly ERA-Interim reanalysis with a horizontal resolution of 1.5° [Dataset]. *European Centre for Medium Range Weather Forecasts (ECMWF)* Retrieved from http://clima-dods.ictp.it/regcm4/EIN15/

ESA. (2012). The European Space Agency Climate Change Initiative Essential Climate Variable (ESA CCI ECV) surface soil moisture combined product with a horizontal resolution of 0.25° [Dataset]. *European Space Agency*. Retrieved from http://clima-dods.ictp.it/regcm4/SURFACE/

Fan, X., Duan, Q., Shen, C., Wu, Y., & Xing, C. (2020). Global surface air temperatures in CMIP6: Historical performance and future changes. *Environmental Research Letters*, *15*(10), 104056. https://doi.org/10.1088/1748-9326/abb051

Feldman, D. R., Worden, M., Falco, N., Dennedy-Frank, P. J., Chen, J., Dafflon, B., & Wainwright, H. (2022). Three-dimensional surface downwelling longwave radiation clear-sky effects in the upper Colorado river basin. *Geophysical Research Letters*, *49*(4), e2021GL094605. https://doi.org/10.1029/2021GL094605

Gao, X., & Giorgi, F. (2017). Use of the RegCM system over East Asia: Review and perspectives. *Engineering*, *3*(5), 766–772. https://doi.org/10.1016/J.ENG.2017.05.019

Gao, Y., Xiao, L., Chen, D., Chen, F., Xu, J., & Xu, Y. (2017). Quantification of the relative role of land-surface processes and large-scale forcing in dynamic downscaling over the Tibetan Plateau. *Climate Dynamics*, *48*(5), 1705–1721. https://doi.org/10.1007/s00382-016-3168-6

Gao, Y., Xu, J., & Chen, D. (2015). Evaluation of WRF mesoscale climate simulations over the Tibetan plateau during 1979–2011. *Journal of Climate*, *28*(7), 2823–2841. https://doi.org/10.1175/jcli-d-14-00300.1

Ge, J., Qiu, B., Chu, B., Li, D., Jiang, L., Zhou, W., et al. (2021). Evaluation of coupled regional climate models in representing the local biophysical effects of afforestation over continental China. *Journal of Climate*, *34*(24), 9879–9898. https://doi.org/10.1175/jcli-d-21-0462.1

Giorgi, F., Coppola, E., Solmon, F., Mariotti, L., Sylla, M., Bi, X., et al. (2012). RegCM4: Model description and preliminary tests over multiple CORDEX domains. *Climate Research*, *52*, 7–29. https://doi.org/10.3354/cr01018

Grell, G. A., Dudhia, J., & Stauffer, D. R. (1994). Description of the fifth generation Penn state/NCAR Mesoscale Model (MM5). *Tech. Rep. TN-398+STR, NCAR*. https://doi.org/10.5065/D60Z716B

Gu, C., & Huang, A. (2024). The regional climate model version 4.5.0 with the 3D sub-grid terrain longwave radiative effect parameterization scheme [Software]. *Zenodo*. https://doi.org/10.5281/zenodo.12657201

Gu, C., Huang, A., Li, X., Yang, B., & Wu, Y. (2024). Construction of a clear-sky three dimensional sub-grid terrain longwave radiative effect parameterization scheme under isotropic assumption. *Journal of Geophysical Research: Atmospheres*, *129*(4), e2023JD039383. https://doi.org/10.1029/2023JD039383

Gu, C., Huang, A., Wu, Y., Yang, B., Mu, X., Zhang, X., & Cai, S. (2020a). Effects of subgrid terrain radiative forcing on the ability of RegCM4.1 in the simulation of summer precipitation over China. *Journal of Geophysical Research: Atmospheres*, *125*(12). https://doi.org/10.1029/2019jd032215

Gu, C., Huang, A., Zhang, Y., Yang, B., Cai, S., Xu, X., et al. (2022). The wet bias of RegCM4 over Tibet plateau in summer reduced by adopting the 3D sub-grid terrain solar radiative effect parameterization scheme. *Journal of Geophysical Research: Atmospheres*, *127*(21), e2022JD037434. https://doi.org/10.1029/2022JD037434

Gu, H., Yu, Z., Peltier, W. R., & Wang, X. (2020b). Sensitivity studies and comprehensive evaluation of RegCM4.6.1 high-resolution climate simulations over the Tibetan Plateau. *Climate Dynamics*, *54*(7), 3781–3801. https://doi.org/10.1007/s00382-020-05205-6

Guo, J., Huang, G., Wang, X., Wu, Y., Li, Y., Zheng, R., & Song, L. (2020). Evaluating the added values of regional climate modeling over China at different resolutions. *Science of the Total Environment*, *718*, 137350. https://doi.org/10.1016/j.scitotenv.2020.137350

Han, S., Shi, C., Xu, B., Sun, S., Zhang, T., Jiang, L., & Liang, X. (2019). Development and evaluation of hourly and kilometer resolution retrospective and Real-time Surface Meteorological Blended Forcing Dataset (SMBFD) in China. *Journal of Meteorological Research*, *33*(6), 1168–1181. https://doi.org/10.1007/s13351-019-9042-9

Hao, D., Bisht, G., Gu, Y., & Leung, L. R. (2023). Regional and teleconnected impacts of solar radiation-topography interaction over the Tibetan plateau. *Geophysical Research Letters*, *50*(23), e2023GL106293. https://doi.org/10.1029/2023GL106293

Holtslag, A. A. M., De Bruijn, E. I. F., & Pan, H. L. (1990). A high resolution air mass transformation model for short-range weather forecasting. *Monthly Weather Review*, *118*(8), 1561–1575. https://doi.org/10.1175/1520-0493(1990)118<1561:ahramt>2.0.co;2;2

Hu, D., Duan, A., Tang, Y., & Yu, W. (2023). Delayed onset of the tropical Asian summer monsoon in CMIP6 can be linked to the cold bias over the Tibetan Plateau. *Environmental Research Letters*, *18*(11), 114005. https://doi.org/10.1088/1748-9326/acff79

21698996, 2024, 23, Downloaded from https://agupubs.onlinelibrary.wiley.com/doi/10.1029/2024JD042102 by Nanjing University, Wiley Online Library on [19/06/2025]. See the Terms and Conditions (https://onlinelibrary.wiley.com/terms-and-conditions) on Wiley Online Library for rules of use; OA articles are governed by the applicable Creative Commons License

Hu, Q., Hua, W., Yang, K., Ming, J., Ma, P., Zhao, Y., & Fan, G. (2022). An assessment of temperature simulations by CMIP6 climate models over the Tibetan Plateau and differences with CMIP5 climate models. *Theoretical and Applied Climatology*, *148*(1), 223–236. https://doi.org/10.1007/s00704-022-03944-6

Huang, A., Gu, C., Zhang, Y., Li, W., Zhang, L., Wu, Y., et al. (2022a). Development of a clear-sky 3D sub-grid terrain solar radiative effect parameterization scheme based on the mountain radiation theory. *Journal of Geophysical Research: Atmospheres*, *127*(13). https://doi.org/10.1029/2022jd036449

Huang, J., Zhou, X., Wu, G., Xu, X., Zhao, Q., Liu, Y., et al. (2023). Global climate impacts of land-surface and atmospheric processes over the Tibetan Plateau. *Reviews of Geophysics*, *61*(3), e2022RG000771. https://doi.org/10.1029/2022RG000771

Huang, X., Han, S., & Shi, C. (2022b). Evaluation of three air temperature reanalysis datasets in the alpine region of the Qinghai–Tibet plateau. *Remote Sensing*, *14*(18), 4447. https://doi.org/10.3390/rs14184447

Jarvis, A., Reuter, H. I., Nelson, A., & Guevara, E. (2008). The Shuttle Radar Topography Mission (SRTM) 90m digital elevation Database v4.1 [Dataset]. *International Centre for Tropical Agriculture (CIAT)*. Retrieved from https://developers.google.com/earth-engine/datasets/catalog/CGIAR_SRTM90_V4

Jiang, Y., Tang, B.-H., & Zhang, H. (2023). Estimation of downwelling surface longwave radiation for cloudy skies by considering the radiation effect from the entire cloud layers. *Remote Sensing of Environment*, *298*, 113829. https://doi.org/10.1016/j.rse.2023.113829

Karlsson, K. G., Anttila, K., Trentmann, J., Stengel, M., Fokke Meirink, J., Devasthale, A., et al. (2017). CLARA-A2: The second edition of the CM SAF cloud and radiation data record from 34 years of global AVHRR data. *Atmospheric Chemistry and Physics*, *17*(9), 5809–5828. https://doi.org/10.5194/acp-17-5809-2017

Karlsson, K.-G., Anttila, K., Trentmann, J., Stengel, M., Solodovnik, I., Meirink, J., et al. (2020). CLARA-A2.1: Monthly CM SAF cLoud, albedo and surface RAdiation data set with a horizontal resolution of 0.25° from AVHRR data—edition 2.1 [Dataset]. *Satellite Application Facility on Climate Monitoring*. https://doi.org/10.5676/EUM_SAF_CM/CLARA_AVHRR/V002_01

Kiehl, J. T., Hack, J. J., Bonan, G. B., Boville, B. A., Williamson, D. L., & Rasch, P. J. (1998). The national center for atmospheric research community climate model: CCM3. *Journal of Climate*, *11*(6), 1131–1149. https://doi.org/10.1175/1520-0442(1998)011<1131:tncfar>2.0.co;2;2

Lee, W.-L., Li, J.-L. F., Xu, K.-M., Suhas, E., Jiang, J. H., Wang, Y.-H., et al. (2019a). Relating precipitating ice radiative effects to surface energy balance and temperature biases over the Tibetan plateau in winter. *Journal of Geophysical Research: Atmospheres*, *124*(23), 12455–12467. https://doi.org/10.1029/2018JD030204

Lee, W.-L., Liou, K. N., & Hall, A. (2011). Parameterization of solar fluxes over mountain surfaces for application to climate models. *Journal of Geophysical Research*, *116*(D1), D01101. https://doi.org/10.1029/2010jd014722

Lee, W.-L., Liou, K.-N., Wang, C.-c., Gu, Y., Hsu, H.-H., & Li, J.-L. F. (2019b). Impact of 3-D radiation-topography interactions on surface temperature and energy budget over the Tibetan Plateau in winter. *Journal of Geophysical Research: Atmospheres*, *124*(3), 1537–1549. https://doi.org/10.1029/2018JD029592

Li, Y., Gao, Y., Chen, G., Wang, G., & Zhang, M. (2024). Decomposition and reduction of WRF-modeled wintertime cold biases over the Tibetan Plateau. *Climate Dynamics*, *62*(5), 4189–4203. https://doi.org/10.1007/s00382-024-07126-0

Liang, X.-Z., Sun, C., Zheng, X., Dai, Y., Xu, M., Choi, H. I., et al. (2019). CWRF performance at downscaling China climate characteristics. *Climate Dynamics*, *52*(3), 2159–2184. https://doi.org/10.1007/s00382-018-4257-5

Lindberg, F., & Grimmond, C. S. B. (2010). Continuous sky view factor maps from high resolution urban digital elevation models. *Climate Research*, *42*(3), 177–183. https://doi.org/10.3354/cr00882

Liu, Y. Y., Dorigo, W. A., Parinussa, R. M., de Jeu, R. A. M., Wagner, W., McCabe, M. F., et al. (2012). Trend-preserving blending of passive and active microwave soil moisture retrievals. *Remote Sensing of Environment*, *123*, 280–297. https://doi.org/10.1016/j.rse.2012.03.014

Luo, J., Huang, A., Lyu, S., Lin, Z., Gu, C., Li, Z., et al. (2023). Improved performance of CLM5.0 model in frozen soil simulation over Tibetan plateau by implementing the vegetation emissivity and gravel hydrothermal schemes. *Journal of Geophysical Research: Atmospheres*, *128*(6), e2022JD038021. https://doi.org/10.1029/2022JD038021

Ma, M., Ou, T., Liu, D., Wang, S., Fang, J., & Tang, J. (2023). Summer regional climate simulations over Tibetan plateau: From gray zone to convection permitting scale. *Climate Dynamics*, *60*(1), 301–322. https://doi.org/10.1007/s00382-022-06314-0

Moore, I. D., Norton, T. W., & Williams, J. E. (1993). Modelling environmental heterogeneity in forested landscapes. *Journal of Hydrology*, *150*(2), 717–747. https://doi.org/10.1016/0022-1694(93)90133-T

NASA. (2016). The monthly surface downward long-wave radiation form Clouds and the Earth's Radiant Energy System (CERES) SYN1deg_Ed4.1 datasets with a horizontal resolution of 1° [Dataset]. *National Aeronautics and Space Administration*. Retrieved from https://ceres.larc.nasa.gov/data/

NESSDC. (2022). The daily global land surface satellite (GLASS) surface longwave radiation with a horizontal resolution of 0.05° based on the Advanced Very High Resolution Radiometer (AVHRR) satellite observation during 2010–2015 [Dataset]. *National Earth System Science Data Center, National Science & Technology Infrastructure of China*. https://doi.org/10.12041/geodata.4718678.ver1.db

Niu, X., Tang, J., Chen, D., Wang, S., Ou, T., & Fu, C. (2021). The performance of CORDEX-EA-II simulations in simulating seasonal temperature and elevation-dependent warming over the Tibetan Plateau. *Climate Dynamics*, *57*(3), 1135–1153. https://doi.org/10.1007/s00382-021-05760-6

NOAA. (2002). The weekly Optimum Interpolation Sea Surface Temperature (OISST) with a resolution of 1° [Dataset]. *National Oceanic and Atmospheric Administration*. Retrieved from https://psl.noaa.gov/data/gridded/data.noaa.oisst.v2.html

Nogherotto, R., Tompkins, A. M., Giuliani, G., Coppola, E., & Giorgi, F. (2016). Numerical framework and performance of the new multiple-phase cloud microphysics scheme in RegCM4.5: Precipitation, cloud microphysics, and cloud radiative effects. *Geoscientific Model Development*, *9*(7), 2533–2547. https://doi.org/10.5194/gmd-9-2533-2016

Oleson, K. W., Lawrence, D. M., Bonan, G. B., Drewniak, B., Huang, M., Koven, C. D., et al. (2013). Technical description of version 4.5 of the Community Land Model (CLM). *National Center for Atmospheric Research. NCAR technical note NCAR/TN-503 + STR*. Retrieved from https://opensky.ucar.edu/islandora/object/technotes:515

Olyphant, G. A. (1986). Longwave radiation in mountainous areas and its influence on the energy balance of Alpine snowfields. *Water Resources Research*, *22*(1), 62–66. https://doi.org/10.1029/WR022i001p00062

Pal, J. S., Small, E. E., & Eltahir, E. A. B. (2000). Simulation of regional-scale water and energy budgets: Representation of Subgrid cloud and precipitation processes within RegCM. *Journal of Geophysical Research*, *105*(D24), 29579–29594. https://doi.org/10.1029/2000JD900415

Palazzi, E., Filippi, L., & von Hardenberg, J. (2017). Insights into elevation-dependent warming in the Tibetan Plateau-Himalayas from CMIP5 model simulations. *Climate Dynamics*, *48*(11), 3991–4008. https://doi.org/10.1007/s00382-016-3316-z

21698996, 2024, 23, Downloaded from https://agupubs.onlinelibrary.wiley.com/doi/10.1029/2024JD042102 by Nanjing University, Wiley Online Library on [19/06/2025]. See the Terms and Conditions (https://onlinelibrary.wiley.com/terms-and-conditions) on Wiley Online Library for rules of use; OA articles are governed by the applicable Creative Commons License

Pareja-Quispe, D., Franchito, S. H., & Fernandez, J. P. R. (2021). Assessment of the RegCM4 performance in simulating the surface radiation budget and hydrologic balance variables in south America. *Earth Systems and Environment*, *5*(3), 499–518. https://doi.org/10.1007/s41748-021-00249-y

Ren, Y., Gao, X., Liu, Y., Li, Z., & Liu, W. (2023). Assessment and improvement of RegCM 4.6 coupled with CLM4.5 in simulation of land surface temperature in mainland China. *Theoretical and Applied Climatology*, *153*(3–4), 1307–1322. https://doi.org/10.1007/s00704-023-04487-0

Reynolds, R. W., Rayner, N. A., Smith, T. M., Stokes, D. C., & Wang, W. (2002). An improved in situ and satellite SST analysis for climate. *Journal of Climate*, *15*(13), 1609–1625. https://doi.org/10.1175/1520-0442(2002)015<1609:aiisas>2.0.co;2;2

Robledano, A., Picard, G., Arnaud, L., Larue, F., & Ollivier, I. (2022). Modelling surface temperature and radiation budget of snow-covered complex terrain. *The Cryosphere*, *16*(2), 559–579. https://doi.org/10.5194/tc-16-559-2022

Sicart, J. E., Pomeroy, J. W., Essery, R. L. H., & Bewley, D. (2006). Incoming longwave radiation to melting snow: Observations, sensitivity and estimation in northern environments. *Hydrological Processes*, *20*(17), 3697–3708. https://doi.org/10.1002/hyp.6383

Su, F., Duan, X., Chen, D., Hao, Z., & Cuo, L. (2013). Evaluation of the global climate models in the CMIP5 over the Tibetan plateau. *Journal of Climate*, *26*(10), 3187–3208. https://doi.org/10.1175/jcli-d-12-00321.1

Sun, J., Yang, K., Lu, H., Zhou, X., Li, X., Chen, Y., et al. (2023). Land–atmosphere feedbacks weaken the cooling effect of soil organic matter property toward deep soil on the eastern Tibetan plateau. *Journal of Hydrometeorology*, *24*(1), 105–117. https://doi.org/10.1175/JHM-D-22-0074.1

Tiedtke, M. (1996). An extension of cloud-radiation parameterization in the ECMWF model: The representation of subgrid-scale variations of optical depth. *Monthly Weather Review*, *124*(4), 745–750. https://doi.org/10.1175/1520-0493(1996)124<0745:aeocrp>2.0.co;2

Viúdez-Mora, A., Costa-Surós, M., Calbó, J., & González, J. A. (2015). Modeling atmospheric longwave radiation at the surface during overcast skies: The role of cloud base height. *Journal of Geophysical Research: Atmospheres*, *120*(1), 199–214. https://doi.org/10.1002/2014JD022310

Wang, L., Liu, Z., Lang, X., & Jiang, D. (2023). Understanding surface air temperature cold Bias over China in CMIP6 models. *Journal of Geophysical Research: Atmospheres*, *128*(19), e2023JD039515. https://doi.org/10.1029/2023JD039515

Wang, S., Wang, T., Leng, W., Wang, G., & Letu, H. (2022). Toward an improved global longwave downward radiation product by fusing satellite and reanalysis data. *IEEE Transactions on Geoscience and Remote Sensing*, *60*, 1–16. https://doi.org/10.1109/TGRS.2022.3179017

Wang, T., & Wang, S. (2022). Fused global land surface longwave downward radiation dataset (2016–2020, 1h/0.25°) [Dataset]. *National Tibetan Plateau / Third Pole Environment Data Center (TPDC)*. https://doi.org/10.11888/Atmos.tpdc.272700

Wang, X., Pang, G., & Yang, M. (2018). Precipitation over the Tibetan plateau during recent decades: A review based on observations and simulations. *International Journal of Climatology*, *38*(3), 1116–1131. https://doi.org/10.1002/joc.5246

Whiteman, C. D., & Hoch, S. W. (2010). Topographic effects on the surface radiation balance in and around Arizona's meteor crater. *Journal of Applied Meteorology and Climatology*, *49*(6), 1114–1128. https://doi.org/10.1175/2010jamc2353.1

Wu, R., Niu, X., Jing, X., Li, P., Mao, Y., Chen, X., & Wang, S. (2024). Future projection and uncertainty analysis of wind and solar energy in China based on an ensemble of CORDEX-EA-II regional climate simulations. *Journal of Geophysical Research: Atmospheres*, *129*(6), e2023JD040271. https://doi.org/10.1029/2023JD040271

Wu, Y., Hu, X., Li, Z., Cai, M., Lu, M., & Yang, S. (2022). Remote effect of model systematic bias in tropical SST on the cold bias over the Tibetan Plateau. *Climate Dynamics*, *60*(7–8), 2219–2234. https://doi.org/10.1007/s00382-022-06421-y

Wu, Y., Wang, N., Li, Z., Chen, A., Guo, Z., & Qie, Y. (2019). The effect of thermal radiation from surrounding terrain on glacier surface temperatures retrieved from remote sensing data: A case study from Qiyi Glacier, China. *Remote Sensing of Environment*, *231*, 111267. https://doi.org/10.1016/j.rse.2019.111267

Xu, J., Liang, S., Ma, H., & He, T. (2022). Generating 5 km resolution 1981–2018 daily global land surface longwave radiation products from AVHRR shortwave and longwave observations using densely connected convolutional neural networks. *Remote Sensing of Environment*, *280*, 113223. https://doi.org/10.1016/j.rse.2022.113223

Xu, L., Liu, H., Du, Q., & Xu, X. (2019). The assessment of the planetary boundary layer schemes in WRF over the central Tibetan Plateau. *Atmospheric Research*, *230*, 104644. https://doi.org/10.1016/j.atmosres.2019.104644

Yan, G., Jiao, Z.-H., Wang, T., & Mu, X. (2020). Modeling surface longwave radiation over high-relief terrain. *Remote Sensing of Environment*, *237*, 111556. https://doi.org/10.1016/j.rse.2019.111556

Yang, M., Zuo, R., Wang, L., & Chen, X. (2018). Simulation of land surface climate over China with RegCM4.5: Verification and analysis. *Advances in Meteorology*, *2018*, 7960908–7960914. https://doi.org/10.1155/2018/7960908

You, Q., Cai, Z., Pepin, N., Chen, D., Ahrens, B., Jiang, Z., et al. (2021). Warming amplification over the arctic Pole and third Pole: Trends, mechanisms and consequences. *Earth-Science Reviews*, *217*, 103625. https://doi.org/10.1016/j.earscirev.2021.103625

Yu, K., Hui, P., Zhou, W., & Tang, J. (2020). Evaluation of multi-RCM high-resolution hindcast over the CORDEX East Asia Phase II region: Mean, annual cycle and interannual variations. *International Journal of Climatology*, *40*(4), 2134–2152. https://doi.org/10.1002/joc.6323

Yue, S., Yang, K., Lu, H., Zhou, X., Chen, D., & Guo, W. (2021). Representation of stony surface-atmosphere interactions in WRF reduces cold and wet biases for the southern Tibetan plateau. *Journal of Geophysical Research: Atmospheres*, *126*(21), e2021JD035291. https://doi.org/10.1029/2021JD035291

Zeng, X., Zhao, M., & Dickinson, R. E. (1998). Intercomparison of bulk aerodynamic algorithms for the computation of sea surface fluxes using TOGA COARE and TAO data. *Journal of Climate*, *11*(10), 2628–2644. https://doi.org/10.1175/1520-0442(1998)011<2628:iobaaf>2.0.co;2;2

Zhang, Y., Huang, A., & Zhu, X. (2006). Parameterization of the thermal impacts of sub-grid orography on numerical modeling of the surface energy budget over East Asia. *Theoretical and Applied Climatology*, *86*(1–4), 201–214. https://doi.org/10.1007/s00704-005-0209-1

Zhang, Z., Zhou, X., & Li, W. (2002). Preliminary numerical study of topographic effects of the Tibetan Plateau on surface direct radiation. *Acta Meteorologica Sinica*, *16*(1), 51–61.

Zhou, M., Yu, Z., Gu, H., Ju, Q., Gao, Y., Wen, L., et al. (2023a). Evaluation and projections of surface air temperature over the Tibetan plateau from CMIP6 and CMIP5: Warming trend and uncertainty. *Climate Dynamics*, *60*(11), 3863–3883. https://doi.org/10.1007/s00382-022-06518-4

Zhou, P., Shao, M., Ma, M., Ou, T., & Tang, J. (2023b). WRF gray-zone dynamical downscaling over the Tibetan plateau during 1999–2019: Model performance and added value. *Climate Dynamics*, *61*(3), 1371–1390. https://doi.org/10.1007/s00382-022-06631-4

Zhou, X., Ding, B., Yang, K., Pan, J., Ma, X., Zhao, L., et al. (2023c). Reducing the cold Bias of the WRF model over the Tibetan plateau by implementing a snow coverage-topography relationship and a fresh snow albedo scheme. *Journal of Advances in Modeling Earth Systems*, *15*(9), e2023MS003626. https://doi.org/10.1029/2023MS003626

21698996, 2024, 23, Downloaded from https://agupubs.onlinelibrary.wiley.com/doi/10.1029/2024JD042102 by Nanjing University, Wiley Online Library on [19/06/2025]. See the Terms and Conditions (https://onlinelibrary.wiley.com/terms-and-conditions) on Wiley Online Library for rules of use; OA articles are governed by the applicable Creative Commons License

Zhou, X., Yang, K., Jiang, Y., Sun, J., Chen, Y., Li, X., et al. (2022). The influence of bare ground thermal roughness length parameterization on the simulation of near-surface air and skin temperatures over the Tibetan plateau. *Journal of Geophysical Research: Atmospheres*, *127*(21), e2022JD037245. https://doi.org/10.1029/2022JD037245

Zhu, X., Qiu, X., Zeng, Y., Ren, W., Tao, B., Gao, J., et al. (2018). Effects of complex terrain on net surface longwave radiation in China. *Theoretical and Applied Climatology*, *134*(1), 251–264. https://doi.org/10.1007/s00704-017-2272-9

Zhu, X., Wei, Z., Dong, W., Wen, X., Zheng, Z., Chen, G., & Liu, Y. (2019). Projected temperature and precipitation changes on the Tibetan plateau: Results from dynamical downscaling and CCSM4. *Theoretical and Applied Climatology*, *138*(1), 861–875. https://doi.org/10.1007/s00704-019-02841-9

Erratum

The originally published version of this article contained an error in Figure 8. Panels 8e1–8e4 were identical to panels 8d1–8d4. In addition, panels 8e1–8e4 should depict the differences in net surface solar radiation. The errors have been corrected, and this may be considered the authoritative version of record.

21698996, 2024, 23, Downloaded from https://agupubs.onlinelibrary.wiley.com/doi/10.1029/2024JD042102 by Nanjing University, Wiley Online Library on [19/06/2025]. See the Terms and Conditions (https://onlinelibrary.wiley.com/terms-and-conditions) on Wiley Online Library for rules of use; OA articles are governed by the applicable Creative Commons License